Growth and Properties of Ultrathin Epitaxial Layers
D.A. King and D.P. Woodruff, editors.

Chapter 5

Heteroepitaxial metal growth: the effects of strain

Harald Brune and Klaus Kern

Institut de Physique Expérimentale, Ecole Polytechnique Fédérale de Lausanne
CH-1015 Lausanne, Switzerland

1. INTRODUCTION: HETEROEPITAXIAL METAL GROWTH

Epitaxial thin films have attracted considerable attention in recent years in the search for new materials. The growth of crystalline films on a crystalline substrate (epitaxy) offers the opportunity to create metastable structures with novel physical and chemical properties. The structure and the properties of the film can be manipulated by the geometric and electronic structure of the substrate. A topical example is the heteroepitaxial growth of Fe on the Cu(100) surface [1], in which the lattice misfit forces Fe films below a critical thickness to adopt the face-centered-cubic (fcc) structure of the Cu substrate, although under normal conditions Fe has a body-centered-cubic (bcc) structure. The fcc Fe-films are particularly interesting with respect to their magnetic properties [2].

In most cases heteroepitaxy involves lattice mismatch between deposit and substrate that will produce strain in the epitaxial layer. The presence of strain can not only force the heteroepitaxial layer into a metastable "artificial" structure but can also severely affect the layer morphology. When a heteroepitaxial layer is grown, initially a flat surface might result under ideal growth conditions when internal defects are suppressed and the layer adopts a pseudomorphic structure. With increasing thickness the strain energy increases proportional to the coverage and the epitaxial film eventually will find a way to relieve the strain. Usually this occurs by the introduction of defects such as dislocations into the epilayer [3, 4] or by roughening of its surface [5, 6]. Since smooth epilayers with atomically abrupt interfaces are desired for most applications, the understanding and control of strain relief and its influence on the film morphology are of primary importance. In this review we discuss the effects of strain in heteroepitaxial metal growth and give some examples of the

variety of mechanisms nature has invented to relieve strain. The examples are mainly taken from the laboratory of the authors, concentrating on systems which grow phase separated. Systems in which interfacial alloying plays a dominant role are discussed in detail in the Chapter by Besenbacher et al. in this Volume. We illustrate in Section 3 that atomic scale surface probes like STM give unprecedented microscopic insights into growth phenomena and demonstrate that in most cases the scenario of strain relaxation is more complex than suggested by simple continuum models.

While the importance of strain relief for the film structure and morphology has long been studied, the effect of strain on the kinetic processes has hardly been recognized. In molecular beam epitaxy (MBE), in particular for metals, however, thin films are usually grown under experimental conditions far from equilibrium [7] (see also Chapter by Rosenfeld and Comsa in this Volume). Film growth will then be governed by kinetic processes, e.g., adatom diffusion on terraces, along and across atomic steps, as well as the nucleation and dynamics of stable and unstable nuclei. Homoepitaxial systems were believed to be ideal model systems to study these kinetic processes in their pure form, without the complications arising from strain or different surface energies of substrate and film [8]. It was hoped that the knowledge gained for homoepitaxial systems could be simply transferred to heteroepitaxial systems. We recently demonstrated, however, that strain has a dramatic influence on the kinetics of the microscopic processes determining epitaxial growth [9-11]. In paragraph 4 we discuss in detail the effect of strain on the nucleation kinetics and on the interlayer mass transport. We also indicate how these strain effects can be exploited to tailor the growth morphology of the heteroepitaxial film.

2. THERMODYNAMIC GROWTH MODE AND STRUCTURAL MISMATCH

The growth mode of a film is usually classified according to the morphology [12, 13]. In the Frank-van der Merwe growth, also known as layer-by-layer (LBL) growth, the film forms a sequence of stable uniform layers with increasing coverage. In cluster or Volmer-Weber growth three-dimensional clusters of the deposit nucleate directly on top of the bare substrate. An intermediate situation is the Stranski-Krastanov growth in which the deposit grows initially in a few (often only one) uniform layers on top of which 3D-islands are formed. The growth modes are of great technological relevance as uniformity of film thickness and structural perfection are crucial in device fabrication. It is obvious that the growth of well-defined layer structures with abrupt interfaces requires the layer-by-layer growth mode.

In a naive picture the equilibrium configuration of a heteroepitaxial system is determined by the competition between the film-substrate interaction and the lateral adatom interaction in the film, describing the anisotropy of chemical bond strength parallel and perpendicular to the interface. Usual measures of these quantities are the isosteric heat of adsorption V_o and the lateral adatom attraction e_ℓ. Based on simple thermodynamics [14], it was argued that layer-by-layer growth should be observed for "strong" substrates, where the adsorbate-substrate interaction V_o dominates the lateral film interaction e_ℓ "Weak" substrates, on the other hand, should favor 3D cluster growth. Physisorption experiments, designed to test these predictions [15, 16], revealed however, that layer-by-layer growth was restricted to a very narrow intermediate range of substrate strengths. Both small as well as large V_o/e_ℓ values resulted in cluster growth.

A more rigorous thermodynamic treatment for the prediction of the growth mode of heteroepitaxial systems was given by Ernst Bauer many years ago [12]. In the case of a film composed of n-layers the criterion for layer-by-layer growth is given by

$$\gamma_{f(n)} + \gamma_{i(n)} - \gamma_s \leq 0 \qquad (1)$$

with γ_s and $\gamma_{f(n)}$ the surface energies of the semi-infinite substrate and the n-monolayer film and $\gamma_{i(n)}$ the interfacial energy. Eq. (1) is rigorously fulfilled in the trivial case of homoepitaxy, when $\gamma_{f(n)} = \gamma_s$ and $\gamma_{i(n)} = 0$. In the heteroepitaxial case the obvious condition for LBL growth is that $\gamma_f < \gamma_s$. The inequality has to be large enough to fulfill Eq. (1) because in general the interfacial energy has no reason to be negative, because substrate and deposit have different crystallographic structure, or at least different natural lattice parameters; thus in general $\gamma_{f(1)} \geq \gamma_f$ and/or $\gamma_{i(1)}$ are positive and non negligible.

Bauer and van der Merwe [17] have included in $\gamma_{i(n)}$ the n-dependent strain energy of the film. In order to emphasize the role of the structure, Eq. (1) may be also written for each layer of the film as

$$\gamma_{f(n)} + \gamma_{i(n,n-1)} - \gamma_{f(n-1)} \leq 0 \qquad (2)$$

with $\gamma_{i(n,n-1)}$ the interfacial energy between the n-th layer and the (n-1)-th layer of the film. Because the surfaces of the layers n and n-1 consist of the same chemical species, $\gamma_{f(n)} \approx \gamma_{f(n-1)}$ with $\gamma_{f(n)}$ slightly smaller if the n-th layer has a more "natural" structure than the (n-1)-th layer, which it certainly tends to have. However, if the structures of the two layers, n and n-1, differ significantly, the interfacial energy $\gamma_{i(n,n-1)}$ becomes important and of course positive and Eq.

(2) is not fulfilled. We can thus conclude that even if $\gamma_f < \gamma_s$ is fulfilled, but the structure of the first monolayer differs appreciably from that of its own bulk, 3D growth may set in above the first monolayer and the film grows in Stranski-Krastanov mode. The onset of this growth mode may be retarded a few monolayers by long range influences of the substrate, but still there will be no layer-by-layer growth.

The rather restrictive condition for layer-by-layer growth, that the structure of the first monolayer must be almost identical to that of its own bulk, is supported by a molecular dynamics simulation of Grabow and Gilmer [18]. Their result is summarized in a "phase diagram" in Fig. 1. The deposition on an fcc(100) substrate surface only occurs in a layer-by-layer mode for strong substrates $V_o/e_\ell \geq 1$ with negligible structural misfit $m \approx 0$ (thick line). The importance of the structural mismatch is also evident in the phase boundary between the Stranski-Krastanov growth and Volmer-Weber growth which shifts substantially to larger substrate strengths with increasing lattice mismatch.

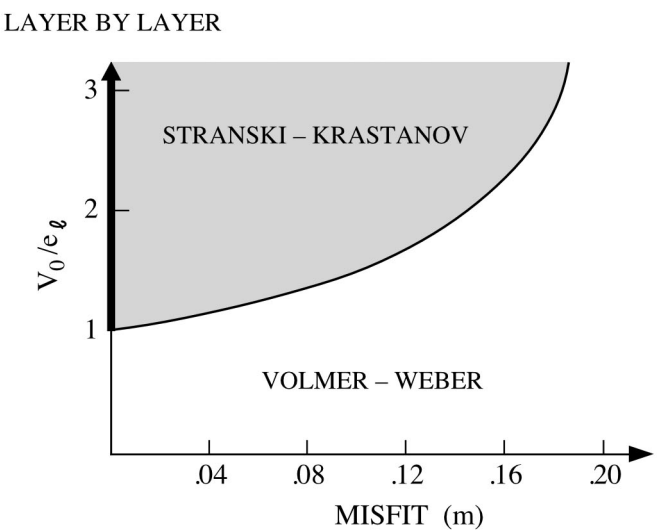

Figure 1. Phase diagram of multilayer growth on an fcc(100) surface in the substrate strength-misfit plane, according to ref. [18].

As already discussed in the introduction film growth from atoms deposited from the gas phase is a non-equilibrium phenomenon governed by the competition of thermodynamics and kinetics. The above considerations are only applicable for growth conditions close to thermodynamic equilibrium, i.e., at high substrate temperature and low deposition flux. With decreasing temperature and increasing flux, i.e., increasing supersaturation, kinetic effects become more

important and finally dominate film growth. In Section 4 we discuss in detail the atomic nature of the most relevant kinetic processes involved in epitaxial growth and explore their sensitivity to strain.

3. STRAIN RELIEF AND STRAIN INDUCED STRUCTURES

Intuitively, it is obvious that the epitaxial growth of one metal on another is easiest, if the structural mismatch between the two metals is negligible. In Fig. 2a lattice matched growth, where the lattice parameter of the substrate a and that of the deposit b coincide, is illustrated. Unfortunately, lattice matched systems are the exception rather than the rule. Usually the crystal structure between substrate and deposit differs and strain effects become important. The usual measure to quantify the strain is the misfit m, defined as the relative difference of the lattice parameters m=(b-a)/a.

The lattice mismatch between film and substrate material in heteroepitaxial growth leads to strain in the film until the film has adopted its bulk geometry through introduction of strain relieving defects. It is important to understand this strain relief, since the defects influence the morphology and the physical properties of the film. Frank and van der Merwe [3] were the first to address theoretically the strain relaxation in an epitaxial system. Based on the Frenkel-Kontorova approach [19] they modeled a monolayer of deposit atoms on a rigid substrate by a one-dimensional chain of atoms coupled by elastic springs subject to an external sinusoidal potential. Later, van der Merwe [20] and Jesser and Kuhlmann-Wilsdorf [21] developed a more sophisticated approach treating the substrate and adlayer as elastic media with an external sinusoidal stress imposed at the interface.

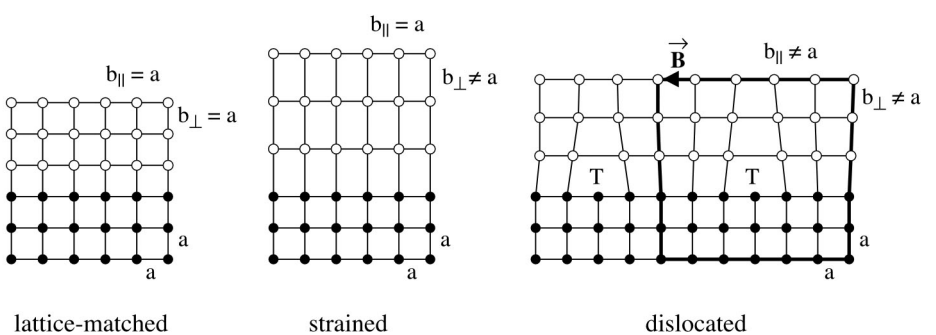

Figure 2. Interfacial structure in an heteroepitaxial system. Shown are lattice matched growth (a), strained coherent growth (b), as well as dislocated growth (c), $\vec{B}$ stands for the burgers vector, and T for threading dislocation. In all cases a layer-by-layer growth mode is assumed.

The theoretical models predicted the existence of a critical misfit $m = m_c$, depending on relative bond strengths, below which a pseudomorphic epilayer can grow (Fig. 2b). In the pseudomorphic state, the film lattice is homogeneously strained into registry with the substrate in the interfacial plane, but can distort tetragonally in the perpendicular direction in order to preserve the volume of the unit cell. The perpendicular lattice constant is given by Eq. (3)

$$b_\perp = a\,(1+m)\,(1+\nu) / (1-\nu) \tag{3}$$

$$E_\nu = 2\,G\,(1+\nu)\,m^2 / (1-\nu) \tag{4}$$

where ν is the Poisson ratio of the deposit material. The elastic strain energy density in the pseudomorphic epilayer is given by Eq. (4), where G is the shear modulus of the deposit material. As the thickness of the pseudomorphic film increases, the elastic strain energy increases and the pseudomorphic epilayer finally becomes unstable at a critical thickness $h = h_c$. Above the critical thickness it costs too much energy to strain the additional deposit layers into registry with the substrate and the strain is partially relieved by the introduction of misfit dislocations (Fig. 2c) [20, 21]. With further increasing film thickness the dislocation density increases until the average strain is eventually reduced to zero, i.e. the adlayer has relaxed towards its natural lattice parameter.

The critical thickness h_c is determined by the elastic constant and the actual misfit m:

$$h_c/z = [\,8\pi\,(1+\nu)\,m\,]^{-1}\;[\,1 + \ln\{\,(1-\nu)\,z / 2\pi d\,\} + \ln\{\,4\,h_c/z\,\}\,] \tag{5}$$

here d is the spacing between the atomic planes on each side of the interface and z is an "intermediate" lattice constant $z = 2ab/(a+b)$. A very similar expression was derived by Matthews and Blakeslee [4] who developed a simple approach based on the stress acting on a pre-existing dislocation in the substrate which threads up through the epitaxial overlayer. For typical metal-metal systems h_c is calculated to vary from below 1 Å ($|m| > 10\%$) up to 10-200 Å for small misfits ($|m| < 2\%$) [21].

Qualitative and quantitative tests of the predictions of the pseudomorphic to strain relaxed transition have been made for numerous heteroepitaxial systems, including semiconductor/semiconductor, oxide/semiconductor and metal/metal interfaces [22]. While epitaxial combinations of semiconductors and oxides were usually found to exhibit critical thickness and residual strain far in excess of prediction, heteroepitaxial metal systems were believed to fit well with the

predictions. This agreement was ascribed to the fact that in metals the lattice offers less resistance to dislocation motion. It was, however, recently shown that also in the case of metal-on-metal systems substantial deviations between theory and experiment exist [23-27]. In the following paragraphs we will describe some of the relevant experiments and discuss the physical origin of this discrepancy.

3.1. Dislocations and the strain relief at hexagonal close-packed interfaces

The continuum model for predicting the pseudomorphic film thickness completely ignores atomic details of the interface structure. Indeed, it has recently been found to fail in the description of hexagonal close packed interfaces [23-25]. This failure is related to the particular structure of close-packed metal surfaces with two favorable adsorption sites, fcc and hcp three-fold hollow sites (Fig. 3a). While these two sites generally have similar adsorption energy, the occupation of bridge or on-top sites is associated with a large energy penalty. Strain at these interfaces can easily be accommodated by the introduction of fcc-hcp stacking faults acting as misfit dislocations (domain walls). Their density is higher or lower than that of the pseudomorphic areas depending on whether the strain is tensile or compressive, respectively. The first type of walls are called heavy, the latter are called light. Depending on the wall crossing energy, the walls may either form a striped pattern (Fig. 4a) or may cross each other yielding a triangular network (Fig. 4b, c). If the wall crossing energy is positive, crossings are energetically unfavorable and consequently a striped domain-wall system is formed. Instead, if the energy cost in the crossing area is negative, crossing becomes favorable and a node network is formed. Examples of both patterns have been observed in a number of metal-metal interfaces [23, 24, 28] and even on reconstructed clean metal surfaces [29-34].

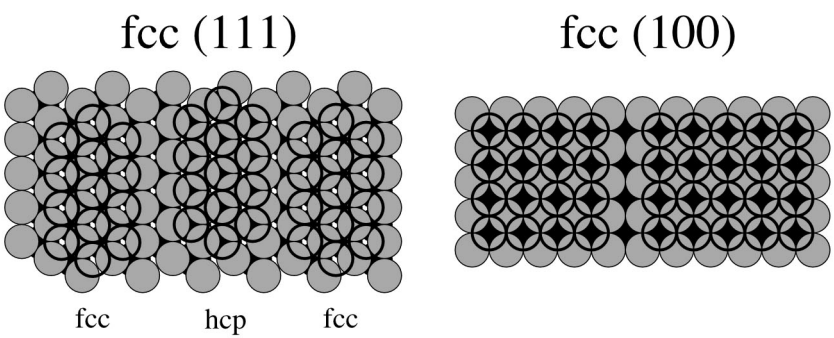

Figure 3. Domain walls in a pseudomorphic adlayer on fcc(111) (a) and fcc(100) surfaces (b). Only in the first case a non-integer phase shift can be produced due to the fcc-hcp stacking fault. While in (a) the right stacking fault represents a light domain wall, the left represents a "super light" wall.

The most extensively studied of these systems is the Au(111) surface with its striped domain wall reconstruction [29, 30, 33]. The reconstruction of this surface is driven by the considerable tensile stress in the outermost layer. It consist in the introduction of a certain density of dense domain walls, or partial dislocations, between alternating fcc and hcp stacking regions. For Au(111) the 4% compression of the first layer is achieved by two partial dislocations per $(\sqrt{3}x22)$-unit cell, each of which inserting one-half extra atom, thus leading to 23 atoms adsorbed on 22 second-layer atoms along the close-packed $\langle 1\bar{1}0\rangle$-directions [33, 35]. Due to the difference in energy, more fcc than hcp sites are populated, giving rise to a pairwise arrangement of the $\langle 11\bar{2}\rangle$-oriented domain walls. Locally, the compression is unidirectional, however, on larger terraces a mesoscopic order of the domain walls is established. The domain walls bend by ±120° with a period of 250 Å [33] forming the so-called *herringbone* structure (see Fig. 4a) which reduces the anisotropy of the surface stress tensor [34].

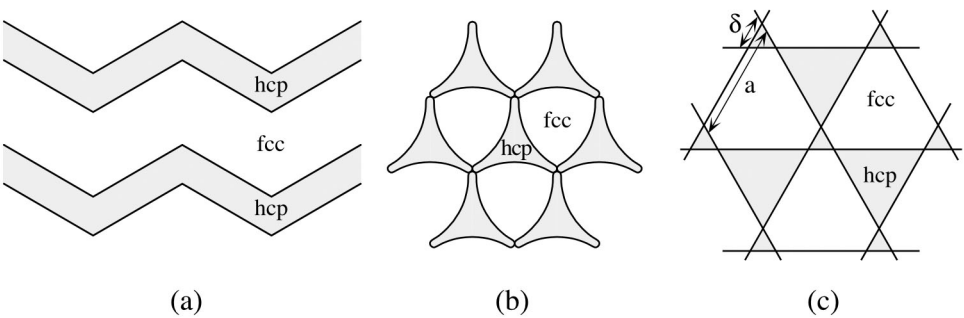

Figure 4. Possible domain wall structures on fcc(111) surfaces. a) striped phase with mesoscopic bending into a herringbone structure. b) and c) trigonal networks with wall crossings.

In epitaxial metal films on close-packed metal surfaces the low energy cost for the formation of the domain walls via hcp-fcc stacking faults essentially drops h_c to zero or just to the first monolayer. As examples we discuss the two epitaxial systems of Cu/Ru(0001) and Ag/Pt(111). Both systems have an atomic size mismatch of roughly 5% (-5.5%, and +4.3%, respectively), in the first system resulting in tensile strain while in the second system the adlayer atom is larger than the substrate atom and the strain is compressive. For both systems the continuum theory predicts a critical layer thickness of a few monolayers, while in experiment only the first monolayer is found to grow pseudomorphic.

In Fig. 5 we show STM images of Günther et al. [24] characterizing the growth of Cu thin films on Ru(0001). The first monolayer grows pseudomorphic; the corresponding STM image (Fig. 5a) only reveals the

hexagonal atomic corrugation with a periodicity identical to that of the substrate. With increasing coverage, however, the pseudomorphic state becomes unstable and the Cu film introduces strain relieving defects.

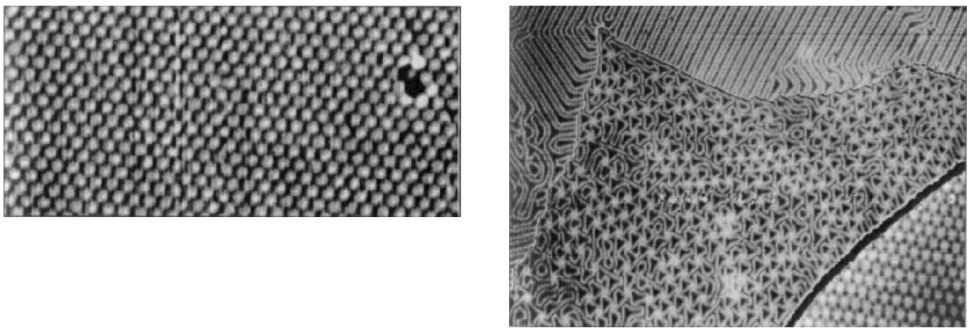

(a) (b)

Figure 5. STM images characterizing a Cu monolayer (a) and multilayer (b) grown on Ru(0001). The nominal coverage of the Cu multilayer is 3 ML. The local thickness varies, however, from 2 ML and 3 ML to 4 ML from top left to bottom right. The image sizes are 7.7 nm x 40 nm (a) and 193 nm x 115 nm (b). From [24].

The corresponding strain relief patterns are clearly visible in the STM images. This is demonstrated in Fig. 5b showing a wedge type sample with Cu coverages increasing from 2 ML and 3 ML to 4 ML from top left to bottom right. The Cu bilayer shows the well known stripe pattern consisting of bright double lines, i.e., heavy domain walls, running along $\langle 11\bar{2} \rangle$. The pattern has a periodicity of ~43 Å along $\langle 1\bar{1}0 \rangle$. High resolution images of the authors revealed the lateral displacement of surface atoms along $\langle 11\bar{2} \rangle$ of 0.8 Å, demonstrating that the domain walls are indeed fcc-hcp stacking faults separating fcc regions (larger domains) from hcp regions (small domains inside the double lines). With increasing thickness the strain relief pattern changes markedly. The 3 ML film shows a domain wall network of triangular symmetry with wall crossings allowing for a more isotropic strain relaxation on a mesoscopic scale. Obviously, the crossing energy has become negative, while it was positive for the bilayer. With further increasing coverage the domain wall network disappears in favor of a moiré pattern characterizing the growth of a weakly modulated incommensurate overlayer.

This strain relief scenario is remarkably similar for the Ag/Pt(111) system, which is under 4.3% compressive strain. In Fig. 6a we show the misfit dislocations which develop upon growth of a 1.5 ML film at 300 K. The second layer reveals again the formation of a striped domain wall phase, where strain is

relieved anisotropically into one of the $\langle 1\bar{1}0 \rangle$-directions per domain which is accomplished by the introduction of a pair of partial misfit dislocations running perpendicular to this direction [23].

a) T = 300 K, Θ = 1.5 ML

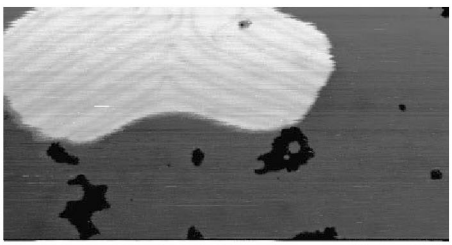

50 Å

b) T_A = 800 K, Θ = 1.5 ML

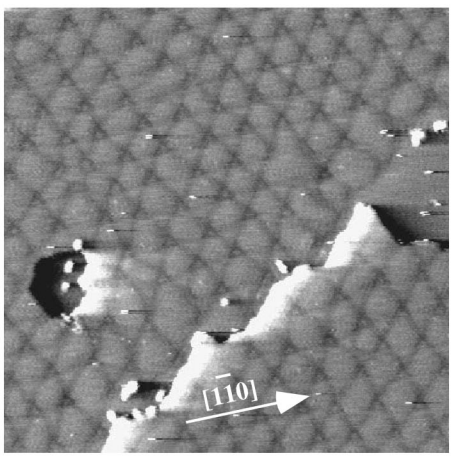

100 Å

Figure 6. Strain relief pattern of a Ag bilayer on Pt(111); integral coverage in both STM images 1.5 ML. At room temperature, the Ag bilayer adopts a metastable striped domain wall phase (a). Upon annealing to 750 K the striped phase transforms into a trigonal network phase (b). From [36].

The striped phase for the second Ag layer on Pt(111) is in fact quite similar to the ($\sqrt{3}$x22)-reconstruction of Au(111) [30, 33, 37] and the Cu bilayer on Ru(0001) [24, 38, 39], discussed above, and has also been observed for Ag films on Ru(0001) [28]. Since the pseudomorphic stacking regions of the Ag layers are under compressive strain, the domain walls in which strain is relieved must represent areas of locally lower density, i.e. they are light walls [23]. Correspondingly the domain walls are imaged as dark depressions while the pseudomorphic domains are imaged bright. This is opposite to the Au(111) reconstruction and Cu/Ru(0001) where the dislocations are areas of locally increased density. Also in contrast to the Au(111) reconstruction and to our original interpretation [23], there are more hcp than fcc sites in this phase, as recently uncovered by X-ray photoelectron diffraction [40]; the large domains are hcp stacking regions while the small domains inside the double lines are fcc stacked. Notice that, in agreement with this finding, in Fig. 6a, the narrow areas are imaged lower by 0.09±0.02 Å than the wider ones. This is in accordance

with the fact that fcc areas within the Au and Pt reconstruction have been imaged lower than hcp regions by about the same amount (0.08 Å and 0.09±0.02 Å for Au and Pt respectively) [32, 33].

The 1st Ag layer on Pt(111) is perfectly flat as demonstrated in Fig. 6a where the tip clearly resolves the dislocations on the second layer while the first layer is imaged flat. This demonstrates that the first layer, when almost completed, is bare of dislocations and hence pseudomorphic [41], analogous to the Cu/Ru(0001) system. The dislocations on the second layer appear dark in the STM topographs. Since atoms in dislocations are adsorbed on bridge sites this STM contrast is inverted to the geometry expected from a simple ball model. There are two ways to explain this STM contrast. The first is based on a reduced density of states at dislocations according to their reduced atomic density. The second evolved from Embedded Atom Method (EAM) calculations for Ag/Ru(0001), suggesting substrate buckling, which was not found in Effective Medium Theory (EMT) calculations for Ag/Pt(111) [42].

The striped phase of the second Ag layer on Pt(111) is metastable. Upon annealing to $T \geq 700$ K (or growth at $T \geq 500$ K) it converts into the equilibrium structure which is a trigonal network where the partial dislocations cross, allowing for more isotropic strain relieve [23]. With this transformation the population of sites also changes to the favor of fcc stacking as expected from their generally higher binding energy. Since the subsequent layers grow in fcc stacking with respect to the second layer, the growth or annealing temperature of the second layer determines whether the whole Ag film grows with or without stacking fault with respect to the Pt(111) substrate [40]. The triangular network shown in Fig. 6b is an example for isotropic strain relief still exhibiting different areas for fcc and hcp stacking. This is realized by shifting one class of domain walls relative to the crossing point of the two others so that crossing of all three domain walls does not occur (see also the model in Fig. 4c). The offset δ generates the small triangles characterizing the structure in Fig. 6b and allows for an optimized ratio between fcc and hcp stacking areas A, according to Eq. (6), and thereby accounts for the actual energy difference between both sides.

$$A(fcc) / A(hcp) = [1 + 2(\delta/a) - 2(\delta/a)^2] / [1 - 2(\delta/a) + 2(\delta/a)^2] \quad (6)$$

Trigonal networks of the type discussed above are found in a number of epitaxial systems, e.g., in surfactant mediated growth of Ge on Si(111) [43], for Na adsorption on Au(111) [44], and for the β phase of Ga on Ge(111) [45, 46]. In all these cases the systems try to increase their fraction of ideal stacking with respect to the faulted one. For Na/Au(111) and Ga/Ge(111) the domain walls are crossing in one point. In the alkali-metal case, therefore, the domain walls bend

and thus incline alternating smaller (hcp) and bigger (fcc) triangles (see Fig. 4b). In the latter case, the domain walls have different width, which allows for bigger fcc areas.

The symmetry of the domain wall pattern changes from uniaxial to quasi hexagonal for Ag films thicker than 2 ML grown at 300 K. The third monolayer (see Fig. 7) exhibits a periodic structure consisting of hexagonally arranged protruding areas surrounded by darker lines which again mark well localized partial dislocations. The space in-between these hexagons is again devided by partial dislocations although less clearly visible in the STM topographs.

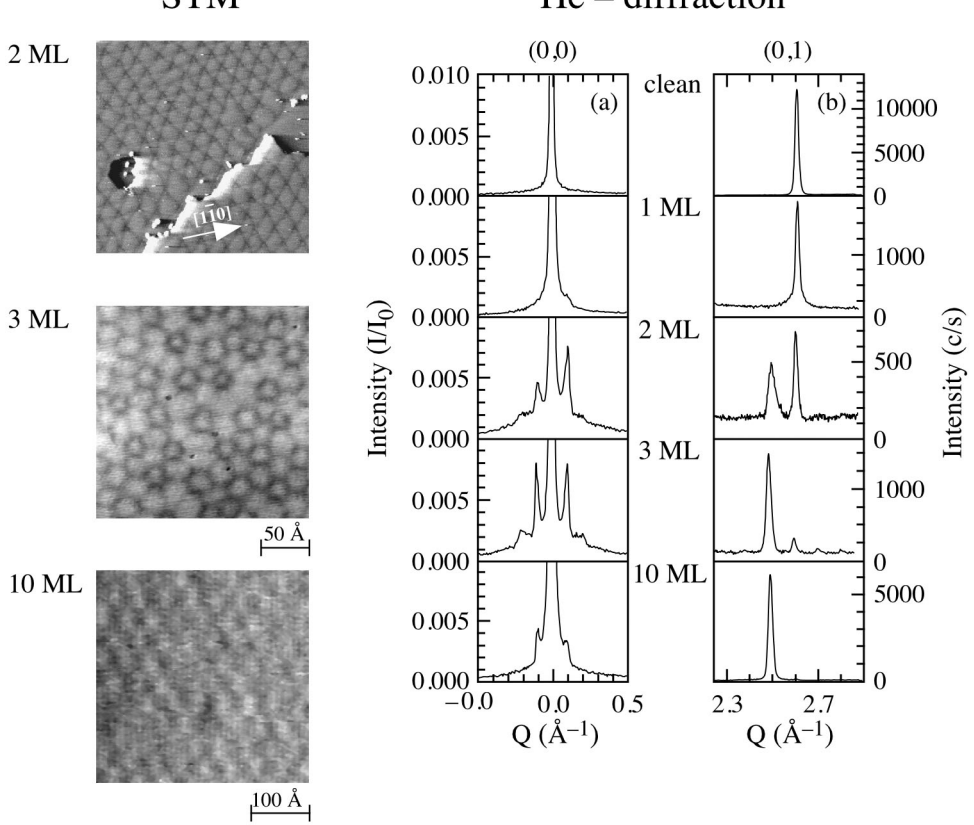

Figure 7. Transition from a domain wall phase to a weakly modulated incommensurate phase with increasing layer thickness of Ag films on Pt(111). On the left hand side we show STM images and on the right hand side the corresponding He diffraction pattern. The He-wavelength was $\lambda = 1.02$ Å. STM images from [36], He diffraction data from [47].

The unit cell of the third layer is a rhombus quite similar to that of the trigonal dislocation pattern characterizing the equilibrium structure of the second layer. Therefore the striped phase of the second layer is unstable towards transformation into a hexagonal dislocation network upon covering it with an additional Ag layer at 300 K. The hexagonal domain wall network persists up to about 10 ML thick films (see Figs. 7). Notice, however, the decrease in image contrast at 10 ML which is associated with less well localized domain walls indicating a transition to a moiré like phase. Thicker films transform into a weakly modulated structure with Ag(111) interplanar lattice constant. This transition in film structure from a misfit dislocation network to a weakly modulated incommensurate structure has also been detected in high resolution He-diffraction measurements [47]. On the right hand side of Fig. 7 we show that up to 3 ML the diffraction spectra exhibit a splitting of the (0,1) diffraction beam characteristic for a dislocation network with its (1x1) pseudomorphic domains and the localized strain relief in narrow domain walls of lower density (this splitting is seen up to 8 ML, not shown here). At a Ag film thickness of 10 ML and above no splitting of the (0,1) diffraction peak is detectable; only one diffraction peak corresponding to an interplanar lattice constant of 2.89Å is measured indicating the growth of Ag layers with bulk Ag(111) structure.

The transition from the pseudomorphic monolayer through a series of domain wall structures with more or less localized strain relief to a weakly modulated moiré phase with increasing film thickness can be understood qualitatively within the simple Frank-van der Merwe picture discussed above [3]. The elastic strain energy increases proportionally to the film thickness. For the monolayer the elastic energy is smaller than the energy to relax the film and the adlayer adopts a pseudomorphic structure. As the thickness and associated strain energy increase, the film relaxes gradually to its natural bulk structure. Initially this is achieved through introduction of hcp-fcc stacking faults, where the strain is locally relieved. At close packed interfaces the introduction of these defects is energetically favorable. However, the domain wall structures still contain substantial residual in-plane elastic distortions. By the gradual transition from the anisotropic striped or trigonal structures to hexagonal networks with larger domain wall widths the residual in-plane strain is progressively lowered. Finally the relaxation is completely isotropic with no in-plane strain resulting in weakly modulated incommensurate structure (moiré) with the bulk lattice constant of the film.

It is, however, important to note that the discussion of the strain relief structures in the framework of the Frank-van der Merwe model is largely simplified. In this model the substrate is assumed to be rigid and the entire relaxation is occurring in the adlayer. Although this might be a reasonable

assumption for rare gas adlayers on metals or graphite it is certainly less adequate for metal-on-metal systems. In these systems the adsorbate-substrate interaction is of the same order of magnitude as the lateral interactions in the film and in the substrate. It is thus natural to assume that not only the film atoms relax at the interface but also the substrate atoms, i.e. the substrate acts as flexible elastic lattice. There is indeed compelling theoretical evidence that this is the case. It is a challenging but not impossible experimental problem to measure quantitatively the atomic distortions in the substrate upon interface formation. Recent STM studies of Ag growth on Ru(0001) in combination with EAM-calculations [28], and of Pb/Cu(111) in combination with EMT-calculations [48], suggest a flexible response of the metal substrate surface; the evidence from the STM data was, however, only indirect since the correlation of imaging and geometric height can even for metals be not trivial. Direct evidence might come in the future from crystallographic studies using x-ray diffraction which can access buried interfaces [49].

3.2. Strain relief mechanisms at interfaces with square symmetry

The strain relief mechanism via fcc-hcp stacking faults is symmetrically impossible at interfaces with square symmetry because there are no different sites with similar adsorption energy (see Fig. 3). For these interfaces many experimental studies have been reported which seem to be in agreement with the predictions of the simple continuum model [22]. We have recently demonstrated, however, that also for these systems atomic details of the interfacial structures have to be considered, which can result in novel strain relief mechanism and substantial deviations from the "Matthews picture". In this paragraph we present again STM results for the strain relief scenarios for two metal-on-metal systems with misfit of opposite sign; i.e., we will compare the strain induced structures of compressively strained Cu films on Ni(100) (m = 2.4%) with those of Cu layers on Pd(100) which is under -7.2% tensile strain.

In Fig. 8 we show a series of STM images characterizing the Cu multilayer growth on Ni(100) at 350 K. Already in the submonolayer range at coverages of about 0.25 ML (not shown here) long protruding stripes appear at the islands which have a typical size of 60 - 80 Å. The stripes protrude by about 0.6 Å, have a width of ~6 Å (which is the typical STM-imaging width of a single atom [50]) and traverse the entire islands. At a coverage of one monolayer the whole surface is covered by a network of stripes (see Fig. 8a). The stripes all have the same width and are all running along $\langle 1\bar{1}0 \rangle$ with an equal probability for the two orthogonal domains. This pattern is maintained up to coverages of about 20 monolayers. The width of the stripes grows linearly with the coverage. Their density and their average length, on the other hand, remain constant in this

coverage range. Note, the stripes do neither cross each other nor coalesce.

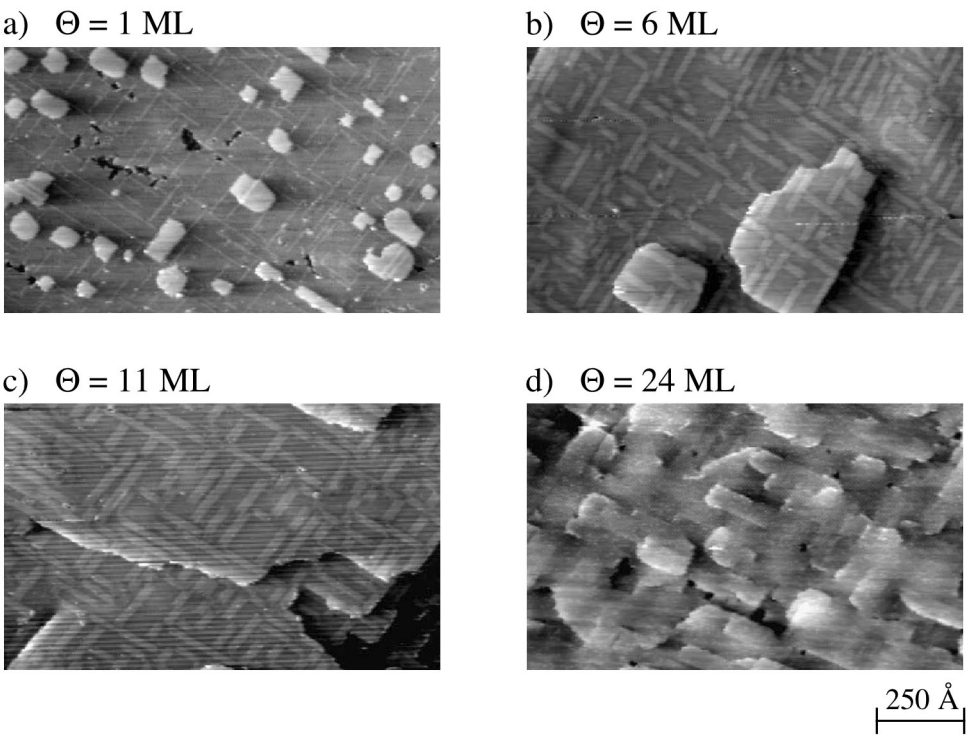

Figure 8. STM images characterizing the multilayer growth of Cu on Ni(100) at 350 K. From [26].

In ref. [26] we have introduced a simple model which accounts for the experimental observations. It is motivated by the fact that the compressive strain at the fcc(100) surface is highest in the close-packed $\langle 1\bar{1}0\rangle$-directions. Therefore, intuitively it could be expected that chains of atoms are squeezed out from the adlayer and create protruding stripes. Due to the square symmetry, these stripes have to form with equal probability in both $\langle 1\bar{1}0\rangle$-directions, perpendicular and parallel to the substrate step edges. The simplest way to generate such stripes is to shift Cu atoms from their four-fold hollow site to the two-fold bridge site (see Fig. 9a). Such a bridge site atom has a reduced number of nearest neighbors in the substrate but it gains binding energy in the adlayer since it is six-fold coordinated there. There are two nearest neighbors within the $\langle 1\bar{1}0\rangle$ atomic chain and, in addition, four lateral neighbors with a binding length which is only about 10 % larger. More importantly, the protruding atoms gain lateral freedom of expansion and the film can partially relieve its strain.

Obviously, this lateral freedom of expansion together with the increased lateral coordination overbalance the lowered binding energy to the substrate.

An important experimental observation is the fact that stripes neither cross nor coalesce at all coverages below about 20 ML (see Fig. 8). This behavior is easy to understand in the proposed model. There are two domains of bridge sites on the square fcc(100) surface representing the two symmetrically equivalent directions of the stripes. At their potential junction, two orthogonal stripes are always separated by $1/\sqrt{8}$ of a lattice constant (i.e. $1/2$ nearest neighbor distance) rendering crossing impossible (see Fig. 9). Coalescence is also unlikely as the distance between two parallel stripes is given by the lattice constant of the Ni substrate and the merging of two stripes would block further transverse relaxation. Therefore, at higher coverages one can find neighboring parallel stripes which have a smaller width than the other stripes at the same image (see Fig. 8 , Θ = 11 ML). Only at high coverages close to 20 monolayers, where almost all of the surface is covered by relaxed stripes, neighboring as well as orthogonal stripes merge and thereby form a high density of bulk dislocations.

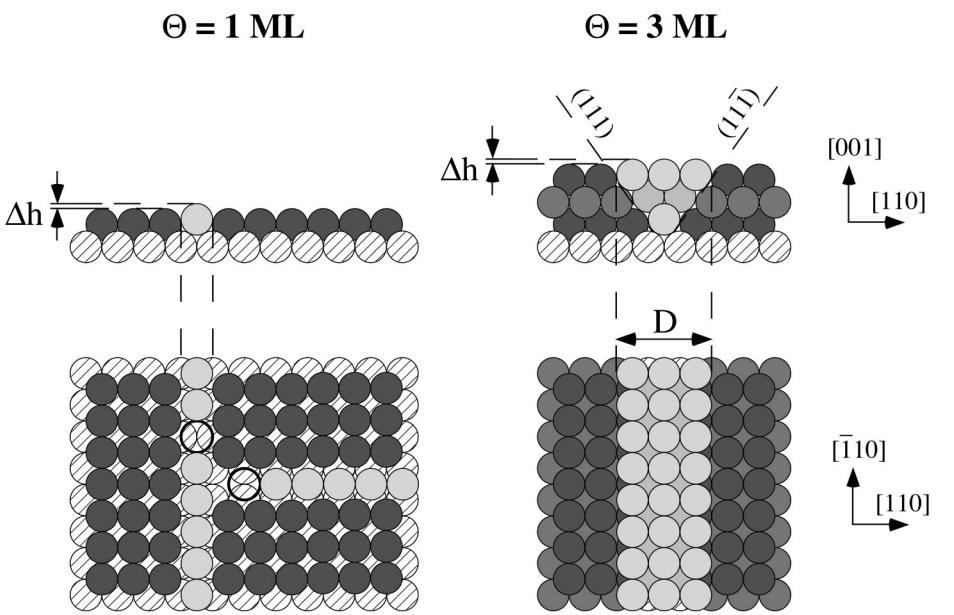

Figure 9. Internal faceting model describing the appearance of the stripes in the Cu mono- and multilayers on Ni(100). The shaded circles represent the substrate atoms (Ni). The "dark atoms" (Cu) are placed at the fourfold hollow sites in pseudomorphic geometry. The "light atoms" (Cu) form the stripes and are placed at the twofold bridge sites. In the monolayer case one can clearly see the two orthogonal domains of bridge sites which renders crossing of the stripes impossible. From [26].

Fig. 9 also shows the model for the trilayer film. The height Δh is independent of coverage. Considering the most simple case of a hard sphere model, one obtains $\Delta h = 0.4$ Å for the example of Cu on Ni. The width D depends on the coverage, i.e., for one monolayer the stripes are exactly one atom wide, for two monolayers two atoms and so on. While the atoms, situated at the hollow sites (dark colored atoms), grow essentially pseudomorphic, the stripe atoms (light colored) can relieve strain at least perpendicular to the stripes [26]. In our model the density of the stripes and their length distribution is determined by the monolayer configuration. The subsequent growth stabilizes the pattern of stripes by the formation of internal {111} facets along the stripes. This is energetically favorable because the strain relaxation takes place by the formation of the highly stable close-packed internal {111} facets.

The growth of thin Cu films on Ni(100) was also studied by Chambers et al. [51] by Auger Electron Diffraction (AED). The ratio of the in-plane to vertical lattice constant (transverse lattice expansion) was measured, which is directly related to the strain of the film. The authors compared their data with the predictions of the continuum model of Matthews and Crawford [52] (thin solid line). The continuum model predicts a critical thickness of $h_C = 14.8$ Å ≈ 8 ML. Up to this thickness Cu should grow pseudomorphic. Only at coverages above 8 ML the film should relax its strain spontaneously by the formation of bulk dislocations. Chambers et al. interpreted their experimental data as confirmation of the continuum model.

Fig. 10 shows clearly that the AED data are much better described by the *internal (111) faceting* model than by the continuum model. Using the *internal faceting* model and the STM data we have calculated the mean values of the transverse lattice expansion. The fraction of the relaxed stripe volume is determined by adding up the stripe coverage in the individual layers as determined by the STM measurements. The relative weight of the individual layers for the AED experiment has been accounted for by the simple ansatz $I = I_0 \exp(-\Theta/\Theta_0)$ using an attenuation factor of $\Theta_0 = 7$ ML. Assuming the stripe atoms are fully relaxed and the copper between the stripes is pseudomorphically grown, one obtains the dashed line in Fig. 10. However, it is likely that the copper close to the stripe boundary is not perfectly pseudomorphic but partially relaxed. It is reasonable to assume (see inset in Fig. 10) that the additional relaxation at the stripe boundary, $\lambda(\Theta)$, depends linearly on the coverage. With $\lambda(\Theta) = 0.2\ \Theta$ [in atomic distances], we obtain the thick solid line in Fig. 10 which is in excellent agreement with the data of Chambers et al. This implies that most of the copper between the stripes is pseudomorphic and the film relieves its strain gradually in a layer-by-layer fashion.

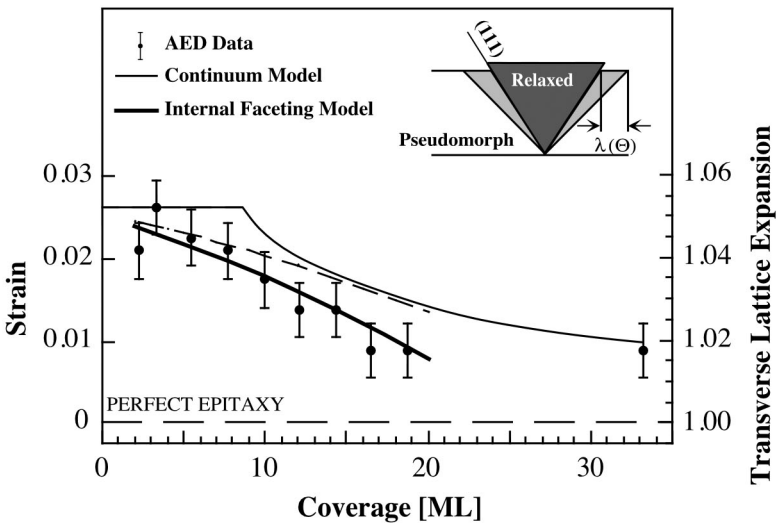

Figure 10. Comparison of the internal faceting model (thick solid and dashed line) and the continuum model of Matthews and Crawford [52] (thin solid line) with the AED data of Chambers et al. [51] (filled circles). Dashed line - internal faceting model with only copper in the stripes being fully relaxed. Thick solid line - copper in the stripes and close to the stripe boundary relaxed; see text. From [26].

A particular strain relief scenario for the heteroepitaxial growth of fcc metals under tensile strain on (100) surfaces of fcc or bcc metals has been predicted many years ago. As early as 1924, Bain [53] suggested that above a critical biaxial expansion of the lattice constant in the (100) plane a fcc solid may transform spontaneously into a bcc or bct (body-centered-tetragonal) phase through relaxation of the interlayer spacing along the perpendicular c-axis (see Fig. 11). The Bain deformation involves the smallest principal strains for the martensitic fcc - bcc (bct) transformation. It appears thus plausible that by pseudomorphic growth on (100) metal substrates with a lattice constant larger than the natural adlayer lattice constant, fcc metals might be forced to grow in a metastable bcc or bct structure.

Pseudomorphic Cu layers on (100) surfaces of fcc metals are particularly attractive systems for the search of a Bain transition in ultrathin films. The stable fcc phase (a = 2.55 Å, c = 3.61 Å) of bulk Cu has extensively been studied experimentally and theoretically and the calculated properties from first principles agree well with experiment. Total-energy calculations of tetragonal distortions by Morrison et al. [54] predicted the existence of two additional metastable bulk phases, a bct phase (a = 2.76 Å, c = 3.09 Å) upon applying a large biaxial tensile strain in the (100) plane and a bcc phase (a = c = 2.86 Å)

upon applying in addition hydrostatic pressure. The theoretical work of Morrison et al. stimulated experiments to grow the metastable Cu phases in pseudomorphic epitaxy on Pd(100). This surface has a square unit cell of side a = 2.75 Å and appears favorable to stabilize bct-Cu. LEED experiments of Marcus and coworkers [55] showed that up to about 10 monolayers a flat pseudomorphic Cu film grows on Pd(100) at room temperature. A detailed structural analysis of the 6 ML film revealed a reduced interlayer spacing of h = c/2 = 1.62±0.03 Å consistent with a bct structure.

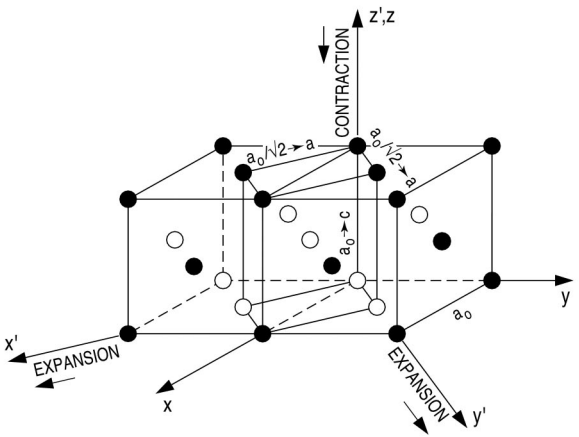

Figure 11. Lattice distortion and corresponding picture of the fcc-bcc (bct) martensitic transition according to Bain [53].

The existence of the two metastable bulk copper phases has however been questioned in a series of theoretical studies [56] subsequent to the work of Morrison et al., in particular the bct phase appeared doubtful and was attributed to an artifact of the computations in ref. [54]. Marcus and coworkers [57] also changed their original interpretation of the LEED analysis of the pseudomorphic Cu film on Pd(100). Based on a strain analysis they suggested that the Cu film should be described as a highly strained fcc phase, and not as a bct phase.

We have recently demonstrated that two pseudomorphic phases of Cu can grow on Pd(100). Below a critical thickness Cu continues the fcc stacking of the Pd substrate with a c-constant of 3.7 Å. Above the critical thickness the c-axis relaxes spontaneously and a structure with reduced lattice constant c = 3.10 Å is formed [58]. The critical coverage for the onset for the growth of the latter phase increases from 1 monolayer at 300 K to 3 monolayers at 400 K. The Bain transition was assumed to be driven by the total strain energy of the Cu film, which scales with the misfit and the film thickness. The decreasing $(Cu\text{-}Pd)_{fcc}$

misfit with increasing temperature (difference in the thermal expansion coefficients) results in an increased critical film thickness at elevated temperatures. Indeed, the reversible switching between both structures of a 2.4 ML film by variation of the temperature proved the "equilibrium" character of both phases and led us to the conclusion that the relaxed phase is a metastable phase while the low-coverage phase would be strained fcc.

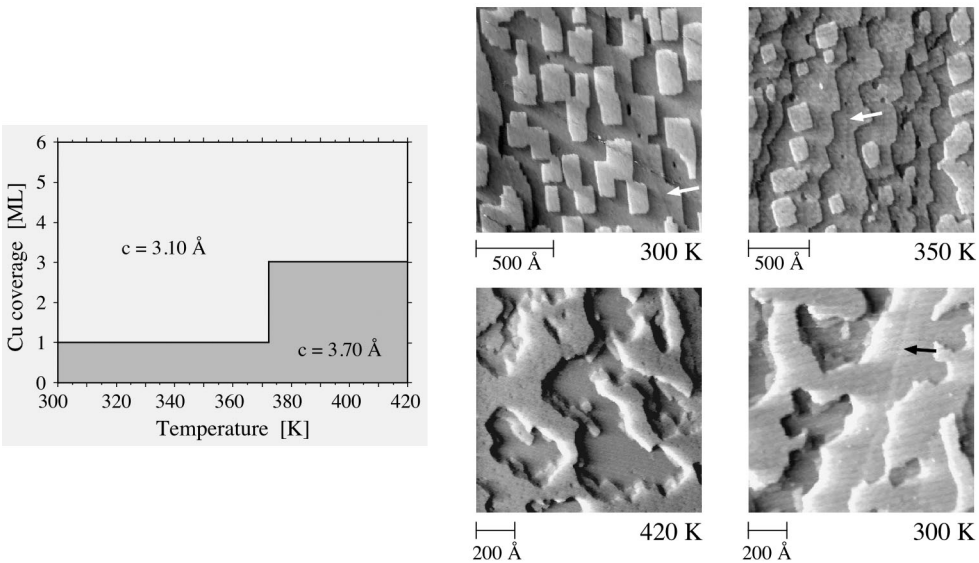

Figure 12. Left hand side: phase diagram of Cu films grown on Pd(100); c is the vertical lattice constant. Right hand side: STM images characterizing the structural change of a 2.4 ML pseudomorphic Cu film on Pd(100) upon annealing and subsequent cooling. (a) Growth morphology of the 2.4 ML film at 300 K. (b) and (c) Morphology at 350 K and 420 K, respectively, and (d) annealing at 420 K and cooling to 300 K. From [58].

Fig. 12 shows that the 2.4 ML Cu phase with reduced c-constant of 3.1 Å has a well shaped island morphology and is unstable towards annealing. The crystal was heated from 300 K to 350 K and 420 K, and cooled back to 300 K; STM images have been taken at the indicated annealing temperatures. At 350 K (Fig. 12b), the onset of island coalescence is observed. The shape of the isolated islands remains nearly unchanged and the small 0.4 Å step at the former Pd substrate step is still present in the STM image (see white arrows), indicating the reduced interlayer spacing and thus reduced c lattice constant of Cu. At 420 K (Fig. 12c), the islands have completely dissolved. Cu has diffused to the step edges or forms large patches on the terraces, no straight Cu step edges are present anymore and the topmost two layers form a percolation network. The drastic morphology change of the Cu film is accompanied by a relaxation of the

whole film. The small 0.4 Å step has vanished upon annealing to 420 K, which indicates the expansion of the Cu interlayer distance. Only single height steps of 1.85±0.1 Å and double height steps of 3.75±0.15 Å are measured, corresponding within experimental error bars to the interlayer spacing in the Cu(100) fcc bulk structure. The formation of large double-layer structures located on the first flat Cu monolayer (which remains entirely intact) demonstrates that the temperature induced phase transition involves massive interlayer mass transport including substantial "upward" motion of Cu. The structural transition is a reversible phase transition as demonstrated in Fig. 12d. Upon cooling down to 300 K, the 0.4 Å step reappears in the STM image (see back arrow in Fig. 12d) indicating the formation of the structure with the reduced interlayer spacing of 1.55 Å.

Motivated by these experimental observations, S. Jeong has studied the structure of Cu films on Pd(100) by ab-initio methods using the norm-conserving pseudo-potential scheme within local-density approximation [59]. His calculation did only reveal one structure with a relaxed lattice constant c = 3.17 Å which he ascribed to a strained fcc structure. There was no evidence for a low coverage structure with a non-relaxed vertical lattice constant. Currently we can thus not unambiguously assign the two Cu structures experimentally observed on Pd(100). It is, however, remarkable that two different pseudomorphic structures with well defined vertical lattice constants exist and that the phase with the relaxed interlayer spacing grows coherent up to a thickness of at least 6 monolayers. In view of the continuum theory this is unexpected. For the Cu/Pd system with its large tensile strain of more than 7% the critical layer thickness for pseudomorphic growth is just one monolayer; i.e., this system documents again the failure of the continuum approach.

3.3. Anisotropic strain relief

Unusually thick pseudomorphic Cu films can also be grown on the anisotropic (110) surface of palladium. At deposition temperatures of about 600 K Cu is found to wet the substrate in a pure step-flow mode. The step-flow mode is maintained also in the Cu multilayer range, up to at least 10 ML as shown in Fig. 13. Up to a coverage of 5 ML the flat Cu films grow pseudomorphically on Pd(110), as evidenced by a sharp (1x1) LEED pattern and the flat imaging by STM.

From a thermodynamic point of view, the growth of thick (1x1) Cu films is difficult to understand, since the total strain energy in the film (7% lattice misfit!) increases linearly with film thickness [60]. Indeed we observe above the critical coverage of 5 ML a partial strain relief of the tensile strain through buckling in the $\langle 1\bar{1}0 \rangle$ direction. This relaxation is detected in the STM images as a striped pattern with the stripes running along $\langle 001 \rangle$ (Fig. 13c). The pattern

corresponds to a buckling with a periodicity of 79 Å, indicating an uniaxial reduction of the tensile strain to 4% along $\langle 1\bar{1}0 \rangle$. The height variation from light to dark stripes is about 0.5 Å. Neither the periodicity nor the height modulation varies considerably when the Cu film thickness is further increased. By LEED, the reconstruction was not detectable due to the limited resolution of our instrument (transfer-width < 200 Å). From the absence of any additional LEED spots and from the STM images it can however be concluded that the Cu atoms are still locked into their positions between the closed packed atom rows of the underlying layer in the ⟨001⟩-directions, while they try to minimize strain by reducing their interatomic distances along the $\langle 1\bar{1}0 \rangle$-direction.

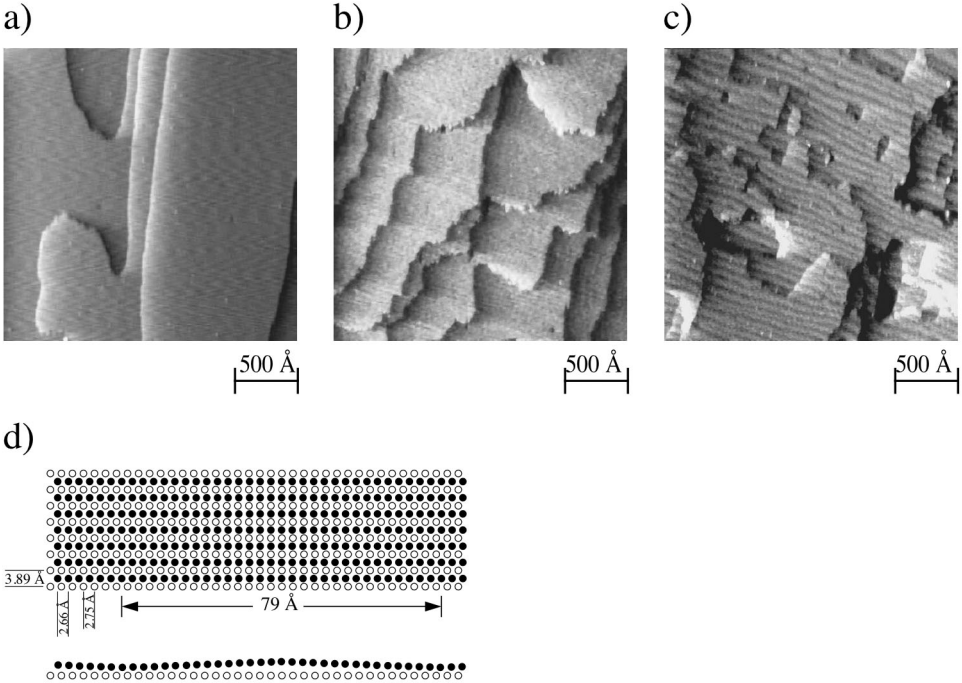

Figure 13. Series of STM images showing the multilayer growth of Cu on Pd(110) at 600 K; 1.1 ML (a), 2.3 ML (b) and 10 ML (c). A model of the uniaxial compression structure of thick Cu layers (here 6 ML) in top and side view is shown in (d). Full circles represent Cu atoms in the 6th layer; open circles: 5th layer Cu atoms. From [61].

Fig. 13d shows a possible model of the reconstructed Cu film surface at coverages above 5 ML. From the observed periodicity of 79 Å it can be calculated that the average interatomic spacing along $\langle 1\bar{1}0 \rangle$ is reduced to

2.66 A. Thus from the 6th layer on, 30 Cu atoms are situated onto 29 atoms of the unreconstructed 5th layer (or the Pd substrate, respectively). Regions where Cu atoms occupy near bridge sites alternate with regions where atoms rest in near fourfold hollow sites, which explains the surface buckling. Obviously, maximum stress relief can not be achieved by reducing the interatomic distances along $\langle 1\bar{1}0 \rangle$ to the Cu bulk value (2.55 A). This may be due to the rigid atom positions in the perpendicular $\langle 001 \rangle$-direction, energetically preventing a further compression. The model shown in Fig. 13d is somewhat oversimplified since the system will try to minimize the occupation of energetically unfavorable bridge sites. In reality, more Cu atoms will be locked into fourfold hollow sites, whereas the atom density will be lower in the bridging regions. Finally it is noted that the density of dislocations (see Fig. 13c) increases with the film thickness, contributing additionally to the relief of stress in the Cu film. Both effects, the uniaxial compression and the dislocation formation, make it possible that Cu layer-by-layer growth continues up to 10 ML, despite the quite large lattice mismatch.

4. EFFECT OF STRAIN ON NUCLEATION KINETICS IN METAL EPITAXY

Very often thin films are grown under experimental conditions far from thermodynamic equilibrium. A typical example is molecular beam epitaxy (MBE), where a high supersaturation is applied to grow films very rapidly from the vapor phase. Under such circumstances thermodynamic quantities, like surface and interface free energies of adsorbate and substrate become less important and the film morphology is governed by kinetic quantities as, e.g., the energy barriers for terrace and interlayer diffusion, or the activation energy for the dissociation of a nucleus of a certain size. These quantities are system specific and their interplay with external growth parameters, like the deposition flux and substrate temperature, determine the resulting film morphology.

The way in which these kinetic quantities and the external growth conditions are linked to the morphology of the growing film is illustrated schematically in Fig. 14. As a prerequisite, however, we need to consider the central result from mean-field nucleation theory. There is a characteristic length scale, which can be identified either with the mean island distance or with the mean free path of diffusing adatoms before they create a new nucleus or are captured by existing islands. This length λ scales as the ratio of the surface diffusion constant D over the flux F to a power of $1/3$ for the case of dimers being stable nuclei (see, e.g., "minimal model" by Villain et al. [62, 63]). The diffusion D is generally described by a prefactor (attempt frequency and geometric factor for the

respective lattice) and a Boltzmann term containing the barrier for surface migration, E_m. For a certain adsorbate-substrate combination, D is therefore determined by the deposition temperature, and together with the deposition flux F it establishes the characteristic length λ.

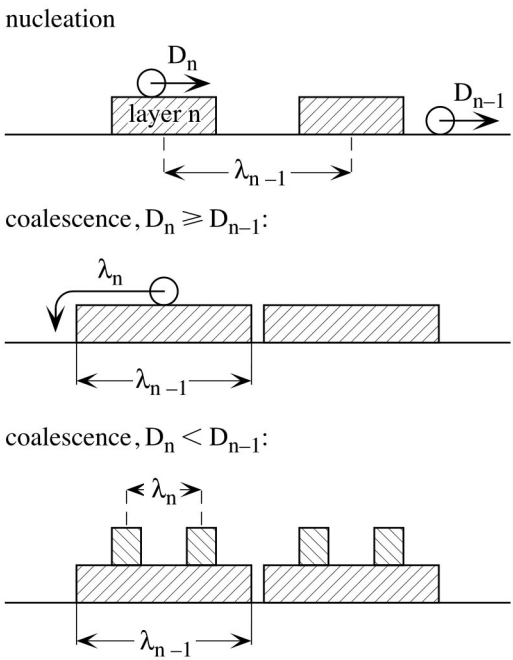

Figure 14. Correlation of the growth morphology to diffusivities on subsequent layers, D_n, D_{n-1}, respectively. The mean island distance λ on each layer equals the island diameter at coalescence and is related to the diffusion rate on the respective underlying layer. For $D_n \geq D_{n-1}$ one has $\lambda_n \geq \lambda_{n-1}$, consequently adatoms deposited onto coalescing islands can reach their perimeter which is the *necessary* condition for layer-by-layer growth, whereas when $D_n \leq D_{n-1}$ islands will nucleate on-top of layer n before coalescence, leading to 3D growth. According to [64].

The generally desired layer-by-layer growth results, when stable nuclei start to form on-top of islands of the growing layer only *after* these have coalesced. In order to prevent nucleation on-top of islands *before* their coalescence, the adatoms impinging onto these islands have to be mobile enough to reach their edges at any time during growth, which evidently is most difficult at coalescence. The mean island size of the n^{th} layer at coalescence equals to the mean island distance, i.e., the characteristic length λ, which is in the way described above, linked to the mobility on the layer underneath, D_{n-1}. In order to enable the adatoms to descend from islands their mobility on-top of the n^{th} layer, D_n, has to be at least D_{n-1}. Therefore, the *necessary* condition for layer-by-layer

growth is that mobilities on subsequent layers, say n-1 and n, obey $D_n \geq D_{n-1}$ [9, 25, 64]. The *sufficient* condition for layer-by-layer growth is that adatoms, after once reached the island edges, are able to descend there. This interlayer diffusion is in general associated with an additional barrier adding to that for terrace diffusion, which we will call ΔE_s.

In homoepitaxy, if no reconstructions are involved, mobilities on subsequent layers are identical, i.e., $D_n = D_{n-1}$. In that case the adatoms are mobile enough to reach the island edge at any time during growth, therefore exclusively the additional step edge barrier determines the film morphology. If the additional barrier is effective at the deposition temperature the system is kinetically limited and grows three-dimensional (3D). If the barrier to interlayer diffusion can be overcome sufficiently frequent, the system is close to thermodynamic equilibrium, where homoepitaxial systems always grow 2D, since the difference in surface and interface free energies $\Delta\gamma = 0$ [65]. The width of the substrate terraces then determines whether step-flow or layer-by-layer growth will result, where only the latter gives rise to oscillations in the step density, detectable by various diffraction techniques, as e.g., Reflection High Energy Electron Diffraction (RHEED) [66-69], LEED [70], Helium Atom Scattering (HAS) [71, 72], and X-ray diffraction [73, 74].

In heteroepitaxial systems strain is involved. In addition, the strain in the topmost layers changes with film thickness. Generally it is decreasing with increasing number of layers, since the film adopts more and more its bulk lattice constant as it grows thicker. In view of the strong variation of strain in the topmost layers, where nucleation takes place, it is obvious to ask whether strain influences the diffusion and dissociation processes involved in nucleation and, if it does, how the growth scenario will then be modified.

In fact there have been several theoretical studies proposing that strain should strongly alter surface diffusion and nucleation kinetics [75-78]. Only very recently, however, the influence of strain on nucleation kinetics could be examined experimentally [9, 10, 25, 36]. A very instructive example is the growth of Ni on Ru(0001) studied by Meyer et al. [25] (see Fig. 15). In this system, the way of strain relief changes from disordered dislocations for the first layer to ordered moiré patterns for thicker layers (see Section 3.1. above). The effect of the varying strain present in these weakly incommensurate phases on nucleation kinetics manifests itself in strongly layer dependent island densities.

The effect of strain on surface and interlayer diffusion has been explored quantitatively for isotropically strained Ag films on a Pt(111) substrate in comparison to relaxed Ag(111) [9, 10, 36]. These experiments demonstrated that strain significantly influences both, surface, and interlayer diffusion. It is thus expected to play the dominant role in determining the film morphology for

kinetically controlled growth. Strain, if isotropic, is simply a variation of the in-plane lattice constant. It is very interesting, also from a theoretical point of view, that both, surface and interlayer diffusion, are rather sensitive to this parameter, and it is tempting to elucidate the physical reason for this.

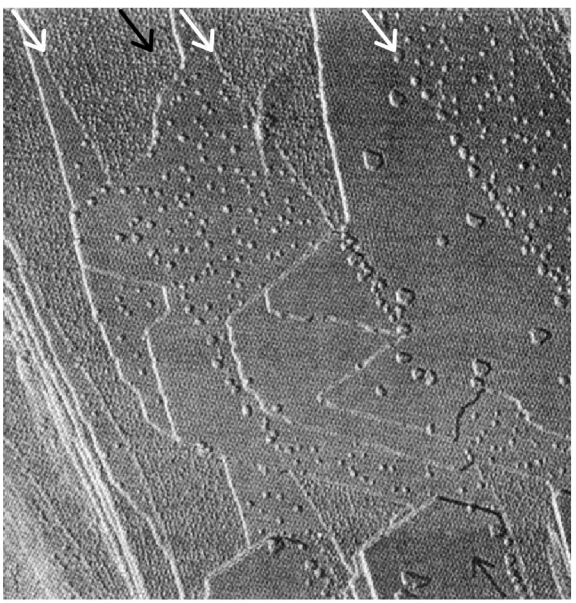

Figure 15. STM image showing a pronounced layer dependence of island densities due to the strain induced restructuring of the Ni film which varies with film thickness. Ni islands have been nucleated by room temperature deposition of 0.05 ML onto a 2.5 ML Ni film on Ru(0001). Between the black arrows there is a single substrate terrace. In going from top to bottom on a line between these arrows the 1st, 2nd, 4th, 3rd, 4th, 3rd, 2nd, and 4th Ni layer are observed, each of them distinguished by its characteristic island density. From [25].

Recently there has been evidence that even for homoepitaxial systems nucleation densities can be layer dependent [79]. For Pt/Pt(111) the adatom induced reconstruction leads to an increase of the island density on the reconstructed substrate, whereas the mobility on the non-reconstructed islands is high, i.e., $D_n > D_{n-1}$ and the most perfect layer-by-layer growth reported so far, results at 650 K. More than 150 almost undamped oscillations are seen in the specular He intensity [71], where a much faster decay of the amplitude was expected without the periodic appearance of the reconstruction.

These very recent results on the effect of strain on nucleation require in general a new concept of layer dependent nucleation kinetics for heteroepitaxial - and even for a certain number of homoepitaxial systems. In the following Section we will review the experimental results on the effect of strain on surface

and interlayer diffusion and finally describe the first steps towards a new concept of layer dependent nucleation kinetics that accounts for these effects.

4.1 Nucleation and surface diffusion

Surface diffusion is one of the central processes involved in thin film growth. The classical method to quantitatively study diffusion on metal surfaces is field ion microscopy (FIM), where the motion of single atoms or clusters on single crystal facets of the FIM tip can be followed at low temperatures on the atomic level [80, 81]. An alternative, although more indirect way to study surface diffusion is to measure island densities that form upon deposition onto a single crystal surface as a function of temperature. The activation energy for surface diffusion is then commonly extracted by application of mean-field nucleation theory [82]. This method recently received considerable attention due to the fact that island densities became accessible in real space on the atomic scale by the availability of scanning tunneling microscopy (STM) [83, 84]. Island densities can also be obtained from other surface sensitive techniques, like electron microscopy [82], electron diffraction [85], and helium atom diffraction [86]. STM has obvious advantages with respect to these methods. The most important of which are that i) island densities can be obtained in-situ in UHV and on terraces without the influence of defects such as steps, and ii) small islands down to single atoms, as well as from very small to extremely high island densities are detectable.

A quantitative study of atomic diffusion requires knowledge on the variation of the island density as a function of substrate temperature. One of the first systematic STM studies of this kind was reported by Stroscio and Pierce for Fe(100) homoepitaxy [87]. (There is an earlier example for Si/Si(100) by Mo et al. [88]. We will, however, focus on examples obtained for metals in the following.) The nucleation of Fe was studied above room temperature, where the description of nucleation generally becomes more complicated than at low temperature due to the increasing number of atomic processes involved. For example assumptions may need to be made about various cluster binding energies [82]. In the case of Fe/Fe(100), the authors later verified that dimers were indeed stable in the temperature range addressed in their former study [89]. For close packed substrates which reveal small energy barriers for diffusion and cluster dissociation this is generally not the case around 300 K. At cryogenic temperatures, on the other hand, dimers are stable nuclei for any system. This reduces a nucleation event to the encounter of two diffusing adatoms and allows for a direct, parameter-free analysis of surface diffusion barriers. It is therefore most convenient to study nucleation at low temperatures which was achieved through the recent development of variable temperature STM [90, 91]. With this

technique, the initial stages of nucleation could be studied on the atomic level, yielding reliable and accurate barriers for surface diffusion on isotropic substrates [9, 92, 93]. Nucleation on anisotropic lattices as, e.g., on fcc(110) [88, 94], or hex-reconstructed fcc(100) surfaces [95, 96] has been studied by several groups. For anisotropic diffusion, as the case on fcc(110) surfaces, a mean-field rate equation treatment was put forward [97]. On anisotropic lattices, however, the analysis of migration barriers is much less straightforward since terrace diffusion, edge diffusion, and sticking to islands may be anisotropic. These effects are *a priori* difficult to discern.

In the following we concentrate on nucleation and surface diffusion on isotropic metal substrates. Since the method applied to study surface diffusion relies on the application of mean-field nucleation theory we first give a brief introduction into the results which are of relevance in the present context. Then we exemplify on hand of nucleation of Ag on Pt(111) how reliable values for the energy barrier and attempt frequency for surface diffusion can be obtained from a careful analysis of the nucleation kinetics. At the end of this paragraph we will discuss the validity and limits of applying nucleation theory in order to extract diffusion barriers in comparison to alternative methods like Kinetic Monte-Carlo (KMC) simulations.

Since the pioneering work on the mechanisms of crystal growth by Frenkel in 1924 [98], Zinsmeister [99], followed by Lewis [100-102], Stowell [103], Venables [82, 104], as well as Stoyanov and Kashchiev [105], Villain, Pimpinelli and Wolf [62, 63], and finally Bales and Chrzan [106], a detailed understanding of the nucleation kinetics during crystal and thin film growth was developed (see, e.g., the Chapter by Venables in this Volume). Much of this theoretical work focuses on the solution of a set of coupled rate equations for the respective island densities. These equations are commonly solved in the *mean-field* assumption that outside the islands the island density immediately takes on its average value. One of the central predictions of mean-field nucleation theory is that the saturation density of all stable clusters n_x depends on the deposition flux F and the adatom diffusion D as follows (for complete condensation being the most relevant case in metal epitaxy, and 2D islands):

$$n_x \propto \left(\frac{D}{F}\right)^{-\chi} \exp\left(\frac{E_i}{(i+2)kT}\right) \tag{7}$$

The exponent χ in the first term on the right hand side of Eq. (7) is $\chi = i/(i+2)$, where i the critical cluster size. In the macroscopic picture critical refers to the cluster size for which the free energy ΔG has a maximum [82]. In a microscopic model a critical nucleus becomes stable upon attachment of a monomer. Here, stable refers to the time scale of deposition, where a stable

island grows more likely than it decays. The Boltzmann term contains the total binding energy E_i of the critical cluster, which, in a simple bond counting model, equals to the number of lateral bonds times their bond energy E_b. By Eq. (7) the critical nucleus size can be inferred from investigation the flux dependence of the island density; from its temperature dependence, the parameters for surface diffusion and cluster binding energies can then be extracted in a second step.

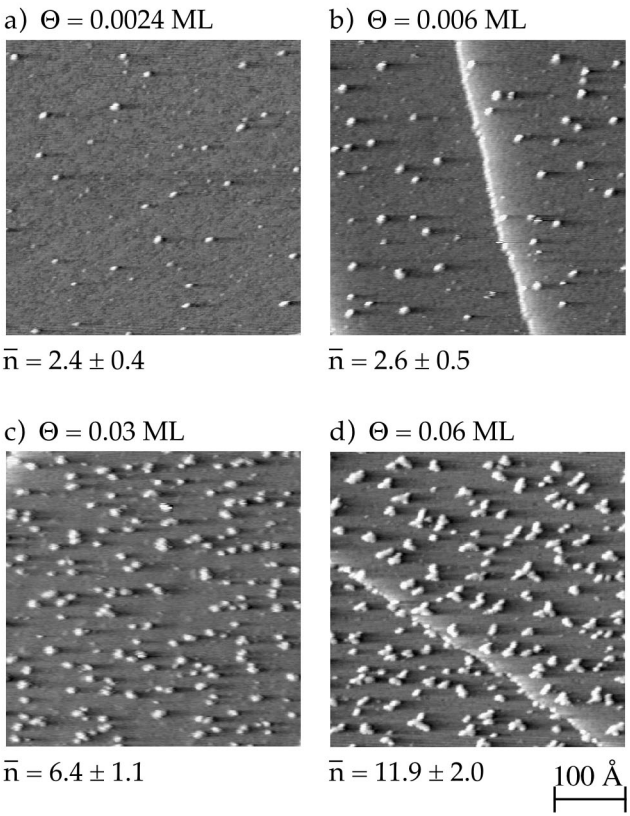

Figure 16. STM images showing the evolution of the island density, size and shape with increasing coverage for Ag deposition (F = 1.1×10^{-3} ML/s) onto Pt(111) at 75 K. Coverages and mean island sizes are indicated. From [92].

In order to get insight into the regimes of nucleation from an experimental point of view, we follow the evolution of the submonolayer film morphology with increasing coverage for Ag deposition onto a Pt(111) surface held at 75 K. Four STM images taken isothermal to deposition are shown in Fig. 16. The very initial stages of nucleation are depicted by Figs. 16a and 16b. The islands,

detectable as bright spots, predominantly constitute dimers and trimers. This is inferred from the mean island size, obtained from the coverage devided by the density, which yields 2.4±0.4 atoms and 2.6±0.5 atoms, for Figs. 16a and 16b, respectively. This is exactly the value expected from nucleation involving dimers as stable nuclei. In course of deposition dimers form until they reach a density similar to that of the diffusing monomers. At this stage, the probabilities for monomers meeting each other and creating new nuclei (dimers), and for attaching to existing dimers (resulting in trimers) become equal. The result is a mixture of mostly dimers and trimers giving rise to the mean island size of about 2.5 atoms. The fact that the mean size does not change from Fig. 16a to 16b, although the coverage has been increased by a factor of about three, is characteristic for the so-called *pure nucleation regime*, since there, additional deposition predominantly results in the formation of new nuclei. Increasing the coverage further by a factor of 5 leads to the transition from nucleation to growth. In Fig. 16c the density is increased by a factor of only two accompanied by a considerable increase in the average island size to 6±1 atoms. Further increase of the coverage by a factor of two leads to exclusive island growth (12±2 atoms per island in Fig. 16d). Thus the last Figure shows the *pure growth regime*, where the island density has saturated, i.e., the islands are dense enough that each arriving film atom has sufficient mobility to reach them with a higher probability than to hit a second mobile adatom and to form a new nucleus.

The set of STM images represented in Fig. 16 completely characterizes nucleation of Ag/Pt(111) at 75 K, as it yields the saturation island density (Fig. 16d) as well as the stable nucleus size (Figs. 16a and b) at this temperature. At higher temperatures, however, direct observation of the mean island size to determine the critical nucleus size is less practical since the pure nucleation regime is then restricted to extremely low coverages. There are various other ways to get information on the critical island size at a certain temperature. One way to detect up to which temperature, e.g., dimers are stable, is to measure the temperature threshold for the onset of Ostwald ripening [107]. For this purpose a large number density of dimers (and also trimers) is produced upon deposition at low temperature, and the island density is monitored by STM as a function of annealing temperature. At the onset of dimer dissociation (or diffusion), the island density suddenly decreases due to more rapid dissociation of smaller islands in favor to larger ones, i.e., due to Ostwald ripening. As an example for this we show Ostwald ripening for Ag/Pt in context with interlayer diffusion in Sect. 4.4. below. There, the threshold for dimer dissociation for annealing periods of half an hour is 100 K, which implies that on the much shorter time scale of deposition, the Ag dimer on Pt(111) is stable up to 110 K.

It is important to notice, that this method to deduce the stable nucleus size

does not rely on nucleation theory. Therefore, it supplies additional information that can serve to independently test, e.g., the flux dependence predicted from this theory. For Ag/Pt it is found indeed that the island densities vary as $F^{1/3}$ for 80 K and 110 K in agreement with Eq. (7) [108]. The island size distributions [108], as well as the absence of a sudden change in slope in the Arrhenius behavior of the island densities (see Fig. 18a below) and the fact that such a change in slope occurs at 110 K [92], all are fully consistent with dimers being the stable nuclei up to 110 K and show the perfect agreement between nucleation theory and experiment.

Fig. 16d also contains information on edge diffusion hidden in the island shape. It is known that island growth at low temperatures can lead to branching caused by the low mobility of adatoms at the island edges. For no edge diffusion at all, ramification takes place into random directions as in Diffusion Limited Aggregation (DLA) scenarios [109, 110]. Before first experimental observations became available [111], low temperature metal epitaxy on close packed substrates was indeed expected to be a realization of DLA. Fig. 16d, and the examples shown in Fig. 17 below, clearly demonstrate, however, that the branches grow into three preferred directions (the crystallographic $\langle \bar{1}\,\bar{1}\,2 \rangle$-directions), leading to Y-shapes for small islands (Fig. 17a and b) and for larger ones to dendrites with a triangular envelope (Fig. 17c). The atomic process at the origin of this particular shape is the asymmetry in diffusion of atoms from 1-fold corner sites towards the two non-equivalent steps present on a hexagonal surface [112, 113]. These two step orientations differ in structure, the A-type steps are {100}-facets, and B-step are {111}-facets, this difference becomes apparent in their different step free energy [114]. For Ag/Pt(111) and Ag/Ag(111) diffusion towards A-steps is activated as soon as terrace diffusion is, since it requires a comparable energy barrier, whereas diffusion towards B-steps is associated with a much higher barrier and therefore inhibited [112]. This leads to asymmetric population of both steps and to branching into preferred directions, as recently been demonstrated [112, 113, 115]. This anisotropy in population of A- and B-steps generally characterizes close packed substrates which implies that dendritic growth is the rule rather than the exception on these lattices [115]. Which step orientation is the preferred one can be system specific. The sign of strain is expected to play a decisive role since it determines which diffusion path is more favorable along the island edge. For square lattices, on the other hand, edge diffusion is generally associated with a barrier comparable to terrace diffusion yielding compact islands from low temperatures on as soon as surface migration and with it aggregation set in [116].

The saturation island density strongly varies with temperature as can be seen from comparison of Figs. 17a-c (notice, the scale of Fig. 17c is twice that of

Figs. 17a and b). Since it directly reflects the adatom mobility it is expected to follow an Arrhenius law. Measured saturation island densities for the example of Ag/Pt at a coverage of 0.12 ML are shown in Arrhenius representation in Fig. 18a in comparison with two mean-field calculations. From the experimental data it is seen that there is a linear regime for temperatures from 110 K down to about 75 K followed by a downward bending of the island densities measured for lower temperatures. The linear regime reflects the expected power law for D/F from Eq. (7). The downward bending to lower island densities is due to the fact that for lower temperatures, diffusion becomes slow with respect to deposition (at $D/F < 10^5$) leading to a certain density of monomers left after deposition. These monomers then either nucleate new islands or attach to existing ones after deposition has been terminated. This nucleation regime is called *post-nucleation*; it is characterized by monotonically decreasing island size distributions, and has been described in detail for Cu/Ni(100) [117]. Square lattices generally reveal higher migration barriers, therefore post-nucleation effects are expected for an extended temperature range on these substrates.

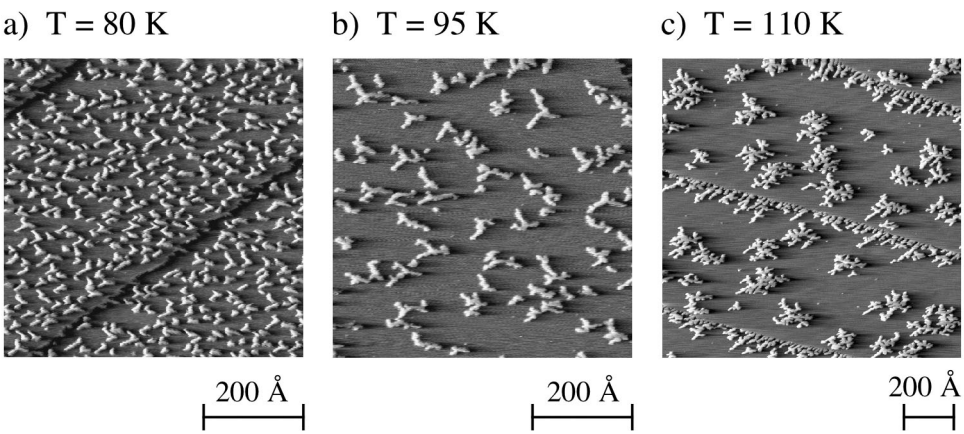

Figure 17. Variation of the saturation island density with temperature and anisotropic island shapes for deposition of 0.12 ML Ag onto Pt(111) at 80 K, 95 K, and 110 K, respectively ($F = 1.1 \times 10^{-3}$ ML/s).

The solid line in Fig. 18a shows the best fit to the experimental data by mean-field rate equations which have been solved self-consistently [106, 108]. Taking into account post-nucleation, the rate equations have been integrated until all monomers were gone, which starts to play a role for $T < 75$ K. The fact, that even at 50 K, apparently all monomers are gone when the island density is measured with STM, is not expected from the diffusion rate at this temperature and the time between deposition and STM experiment. It is presumably due to

the interaction of the STM tip with adsorbed monomers. The influence of the STM tip has been shown to considerably decrease the diffusion barrier for Pt/Pt(111) [93]. Therefore, in our example, the few remaining monomers are probably being attached to existing islands due to the measurement itself. This does not obscure the results since stable nuclei turn out to be unaffected by the measurement.

The mean-field calculation shows excellent agreement with experiment, it has been performed with a migration barrier of E_m = 168 meV and an attempt frequency of $\nu_0 = 6.76 \times 10^{13}$ s^{-1} (notice, $D = {}^1/_3\, \nu_0 \exp(-E_m/kT)$, with the geometric factor being $^1/_3$ since hopping has been assumed to take place from fcc to fcc sites). A self-consistent solution to the mean-field rate equations such as shown in Fig. 18a is certainly the most precise available to date, however, it is mathematically demanding [106]. It is therefore valuable to discuss alternative ways to extract parameters for surface diffusion from the type of data shown in Fig. 18a.

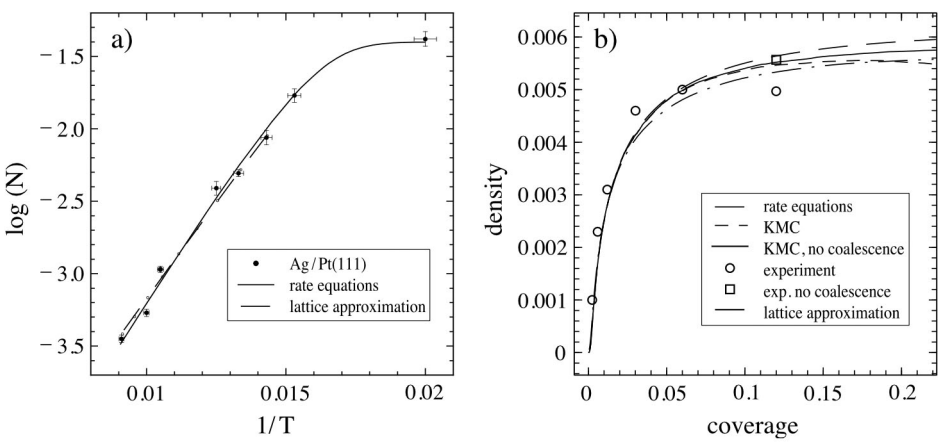

Figure 18. Comparison of experimental island densities for Ag/Pt(111) with calculations from self-consistent and approximate solutions of mean-field nucleation theory and KMC simulations. a) Arrhenius plot of saturation island densities (Θ = 0.12 ML) for the regime where dimers are stable nuclei. b) Island density versus coverage at 75 K. From [108].

The most easy and widely used approach is to apply Eq. (7) to the linear part in the Arrhenius plot, where dimers are stable (i = 1), and extract the migration barrier and the attempt frequency from the slope of the linear regression to the data and its intersection with the ordinate. This far more simple approach yields fairly good agreement with the values obtained from the full analysis. Taking the STM data for 75 K ≤ T ≤ 110 K, where $1 \times 10^5 \leq D/F \leq 4 \times 10^8$, one obtains E_m = 170±10 meV and $\nu_0 = 4 \times 10^{13.0 \pm 0.5}$ s^{-1}. (For the attempt frequency, the

proportionality factor in Eq. (7) has been set to $\eta(\Theta) = 0.2$. This value has been given by Venables, see curve for i = 1 at $\Theta \approx 0.1$ ML in Fig. 6c of ref. [82], and is also obtained in the self-consistent analysis by Bales). Notice, however, that great care must be taken when selecting the data attributed to the linear regime. As can be seen from inspection of Fig. 18a, the calculated curve starts to bend for $T < 75$ K, respectively $D/F < 1x10^5$. We therefore emphasize that only data for $D/F > 1x10^5$ should be analyzed in a linear regression. Thus a slightly lower barrier of $E_m = 157\pm10$ meV ($\nu_0 = 6x10^{13.0\pm0.8}$ s^{-1}) has been obtained when the slope was analyzed including data down to 65 K [92], where it is seen from Fig. 18a that post-nucleation already decreases island densities.

The evolution of the island density with coverage for our example of Ag/Pt(111) at 75 K is plotted in Fig. 18b (compare also STM images in Fig. 16). Again, there is perfect agreement with the self-consistent rate equation analysis. Since the analysis did not account for coalescence, an experimental value at 0.12 ML for the (hypothetical) island density without coalescence has been derived, which can be accomplished, since coalesced islands are discerned by their shape from those that grew from a single nucleus. Fig. 18b also shows KMC simulations performed on a square lattice with the same parameters as in the rate equations. They are in perfect agreement with experiment and rate theory. The results from KMC simulations performed on a hexagonal lattice accounting for the dendritic island shape [108] are hardly discerned from the KMC results shown here. In general, KMC simulations have served as valuable test for nucleation and scaling theories [106, 118-121]. For our example of Ag/Pt, Fig. 18b shows that the self-consistent rate equations are in quantitative agreement with these simulations and both perfectly describe the experiment.

Another common approach is to integrate rate equations of nucleation within certain approximations for the capture numbers σ, significantly reducing the calculational effort [92, 93]. These approximations are compared in Fig. 18b to the exact solutions and KMC simulations discussed above. The capture numbers describe the capability of islands or monomers to capture diffusing adatoms. They generally involve solutions of two-dimensional diffusion problems. This is not the case in the geometrical concept [122] where capture numbers are assumed to scale with the island diameter seen by the approaching monomers. This concept, when applied to fractal islands, yields $\sigma_x = 2+x^{1/1.7}$ (with x being the island size in atoms, the constant of 2 accounts for atoms diffusing towards sites adjacent to the island perimeter). This approximation has successfully been applied to calculate the evolution of island densities with coverage at a single temperature [92]. It has been shown, however, to be inconsistent in so far as it yields a higher slope in the Arrhenius representation of the island densities compared to the slope expected from Eq. (7) [93]. It was noted early that the

geometric concept gives even more inaccurate predictions than constant capture rates [123], which should therefore be preferred as the most simple approximation. A more elaborate approach is obtained from solving the diffusion equation in the lattice approximation [104, 123]. This yields an analytic expression for σ_x (stable islands) that depends only upon coverage. For monomers, on the other hand, a constant value of $\sigma_1 = 3$ corresponding to the geometrical concept can be used for simplicity. The rate equations for monomers and stable islands read for the case of metal epitaxy at low temperatures, i.e., for dimers being stable and immobile and neglecting re-evaporation (compare Eqns. 2.3, 2.5, 2.6. and 2.8 in ref. [82]):

$$\frac{dn_1}{dt} = F - 2\sigma_1 D n_1^2 - \sigma_x D n_1 n_x - F(Ft - n_1) - 2Fn_1 \tag{8}$$

$$\frac{dn_x}{dt} = \sigma_1 D n_1^2 + Fn_1 \tag{9}$$

The terms on the right hand side of Eq. (8) denote the increase of monomer density due to deposition with flux F, their decrease due to the encounter of two diffusing atoms under creation of a dimer associated with the disappearance of the two atoms, the decrease occurring when a monomer is captured by a stable island, and the last two terms denote the decrease caused by direct impingement onto stable islands, respectively monomers. In Eq. (9) the terms on the right hand side account for the increase of stable island density n_x due to creation of dimers, first when two monomers meet by diffusion, and second upon direct deposition onto a an adatom. For sake of comparison with the self-consistent analysis above, coalescence is neglected in Eq. (9); incorporation would add a further term $-2n_x(F-dn_1/dt)$.

The result from numerical integration of these equations within the lattice approximation (see dash-dotted curves in Fig. 18) is seen to compare well to self-consistent rate theory as well as to KMC simulations and experiment (apart from the small deviation in slope). In variance to this result, the lattice approximation has earlier been reported to yield slightly too high values [93]. This discrepancy might be ascribed to a small difference in the equations used by Bott et al., i.e., they did not account for direct impingement onto monomers expressed by the last terms in Eqns. (8) and (9). Note, that coalescence is not very accurately described by the coalescence term, e.g., for 1 ML the island density stays at a finite value.

In summary, the straight forward analysis of island densities by mean-field nucleation theory by means of Eq. (7), when performed for $D/F > 10^5$ and a critical nucleus size of one, allows to determine the energy barriers and attempt

frequencies for surface diffusion with good accuracy. This precision can further be increased when comparing experimental data to self-consistent mean-field theory or to KMC simulations, which both are fully consistent to each other. In addition, nucleation theory has recently been subject of rather direct experimental tests which all underline its validity for isotropic substrates [9, 87, 92, 117]. This has placed its application for extracting parameters for surface diffusion from island densities on a firm basis. Also for anisotropic substrates, a mean-field treatment was put forward [97], and applied to estimate diffusion barriers [94, 95].. For these cases, however, generally more experimental information is needed to discern anisotropic terrace diffusion from anisotropic diffusion around and sticking to the island edges [95, 96]. For this purpose, and generally for cases where many diffusion processes are involved, as well as for island size and distance distributions, KMC simulations are a valid tool for comparison with experimental data and as a check for predictions from mean-field and scaling theories.

4.2. Effect of isotropic strain on surface diffusion and nucleation

Isotropic strain, as it appears in the growth of pseudomorphic heteroepitaxial layers, is the variation of the in-plane lattice constant of the film material with respect to its bulk value. Theoretically, it has been pointed out several times that surface diffusion and thus nucleation should be altered by strain. Two molecular dynamics simulations were proposing that for semiconductor surfaces strain changes adatom mobilities [75, 76]. A theoretical study was explicitly investigating the effect of strain on the nucleation kinetics on vicinal surfaces [77] and there was even the suggestion to apply strain in order to influence the growth kinetics - with the goal to grow linear structures attached to the steps of a vicinal substrate [78]. Only very recently, however, the influence of strain on surface diffusion and nucleation has been addressed experimentally. The experiments showed that the barrier to surface migration on a pseudomorphic Ag monolayer on Pt(111) is significantly reduced with respect to that on a fully relaxed Ag(111) surface. This observation prompts the question whether this effect is indeed due to strain, or rather caused by the electronic adlayer-substrate coupling. Calculations within Effective Medium Theory (EMT) and very recent ab-initio calculations [124, 125] demonstrate that in fact strain is by far dominating electronic coupling. In this Section, we discuss these first experimental and theoretical results on surface diffusion on isotropically strained surfaces.

For the system Ag/Pt(111) there is a strong layer dependence of island densities as becomes evident from inspection of Fig. 19. The three STM images were obtained for low temperature nucleation of Ag on Pt(111), on the first Ag

monolayer grown on Pt(111), and on Ag(111), respectively (see Figs. 19a - 19c).

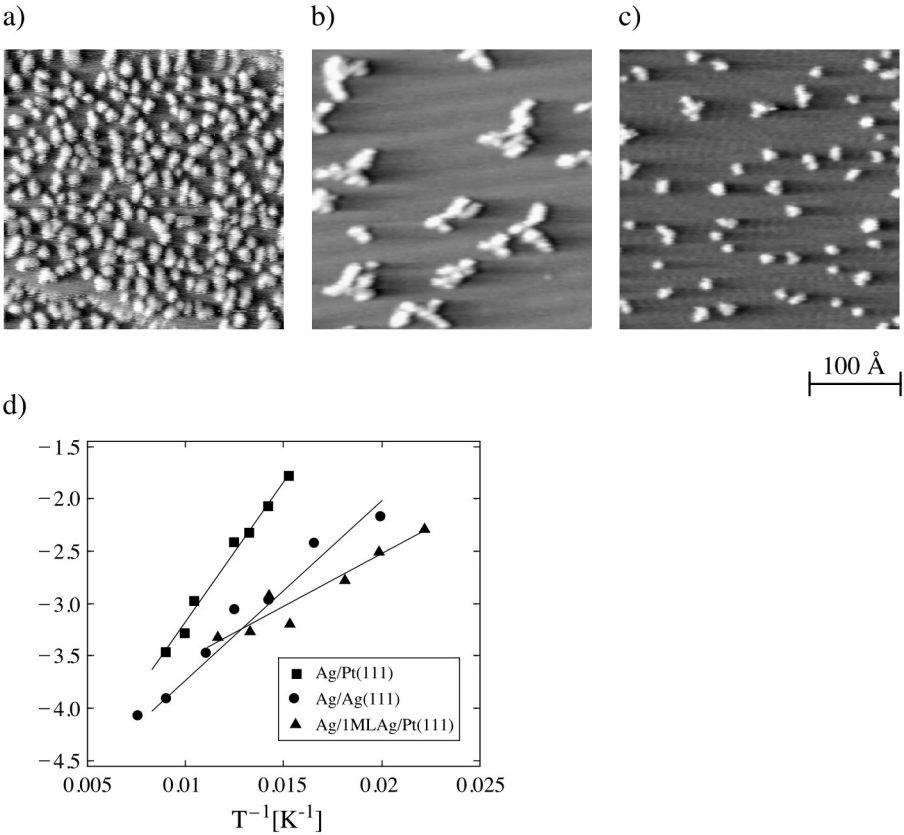

Figure 19. STM images showing the nucleation of submonolayer coverages of Ag on Pt(111) a), 1MLAg/Pt(111) b), and on Ag(111) c), respectively. ((a) T = 65 K; (b) T = 65 K; (c) T = 60 K, size 307x307 Å^2). d) Arrhenius plot of saturation island densities derived from STM for nucleation of Ag on Pt(111) (■), on 1MLAg adsorbed on Pt(111) (▲), and on Ag(111) (●), respectively. From [9].

The lowest island density is observed on the first Ag layer. The structure of this layer is pseudomorphic with respect to the Pt(111) substrate [23, 40, 41, 126]. The Ag interatomic distance in this layer is therefore reduced by 4.3% with respect to the Ag bulk value. The Ag(111) surface has been prepared by deposition of a thick Ag film onto Pt(111) at 450 K and subsequent annealing to 800 K. This yields extended, perfectly flat terraces, giving rise to a single diffraction peak in high-resolution He-diffraction measurements which corresponds to the interplanar lattice constant of bulk Ag(111) of 2.89 Å [47].

The temperature dependence of saturation island densities on these three substrates shows strongly differing slopes, indicative for differing migration barriers (see Arrhenius in Fig. 19d). Nucleation on the pseudomorphic Ag layer is characterized by the smallest slope, followed by Ag(111) and finally by Pt(111). These slopes directly yield the parameters for surface diffusion on these layers, since dimers are stable for the data shown here. This is indicated by the absence of bends in the Arrhenius and has also been verified by dimer annealing experiments. The resulting migration barriers E_m on the different isotropic layers amount to 168±10 meV for Ag/Pt (see preceding Section), 60±10 meV for the pseudomorphic Ag layer and finally 97±10 meV for Ag diffusion on a strain-free Ag(111) surface [9].

The most conspicuous effect uncovered by the STM experiment is the low barrier for Ag diffusion on the pseudomorphic Ag layer compared to unstrained Ag(111). Two effects are conceivable to cause the observed lowering. It may either be due to the 4.3% compressive strain or an effect of the electronic adlayer-substrate coupling. In order to decide which of both is dominant we consider the results from EMT [127, 128] calculations represented in Fig. 20. These calculations have been performed for a Ag atom adsorbed on a periodically repeated 6x6 cell of a 5 layer thick slab; the three upper layers of which were free to relax. The adatom is then pulled over this surface, allowing its position to relax freely in a plane perpendicular to the vector of displacement to find the minimum of total energy in course of this displacement. The diffusion barrier E_m is then determined as the difference in total energy between the transition state (bridge site) and the preferred adsorption site (fcc- or hcp-hollow).

In order to investigate the effect of strain on the diffusion barrier, the Ag(111) slab has been subjected to strain by changing its lateral dimensions while leaving it free to relax in the (111) direction. The EMT results presented in Fig. 20a clearly show that strain has a pronounced influence on migration barriers. For a compression of 4.3% the barrier is lowered from 67 to 40 meV, respectively by 40% This compares well to the experimentally observed lowering. Regarding absolute values, it is known that EMT underestimates diffusion barriers on close packed surfaces [129, 130], however, the order of the calculated barriers is in full agreement with the experimental values for our example [9]. The migration barrier for Ag on a pseudomorphic Ag monolayer on Pt(111), on the other hand, is found in the EMT calculations to be only slightly higher (50 meV) than the strained Ag(111) case. These calculations therefore suggest that electronic effects of the Pt substrate even slightly decrease the effect of strain, at the same time they identify strain as the dominant origin for the observed lowering of the migration barrier.

Rather good absolute values for migration barriers on close packed surfaces have recently been provided by ab-initio calculations, either performed within Local Density Approximation (LDA) or with Generalized Gradient Approximation (GGA). (For a review on ab-initio calculations of surface diffusion see Chapter by Ruggerone, Ratsch, and Scheffler in this Volume.) The barrier for Ag/Pt(111) has been calculated by Feibelman to 200 meV [131], and recently by Ratsch and Scheffler to 150 meV, both in good agreement with the experimental value. For Pt(111) self-diffusion, the theoretical values (380 meV [130], 390 meV [125]) lie above the established experimental result of 0.25 eV [93, 130]. For Ag(111) self-diffusion 100 meV has was calculated by J. J. Mortensen et al. using calculations with GGA [125] in agreement with the LDA value of 90 meV obtained by Ratsch and Scheffler [124] (a slightly higher value of 140 meV was reported in a recent LDA calculation [132]). As in the case for Ag/Pt, also these theoretical numbers are in good agreement with experiment (97±10 meV, see above). Therefore, it is particularly valuable that these more precise calculations are in agreement with the interpretation formerly deduced from the EMT results presented above. Ratsch and Scheffler find reduced diffusion barriers on the pseudomorphic Ag layer on Pt(111), 65 meV, as well as on a compressively strained (by 4.3%) Ag(111) slab, also 65 meV [124]. These values agree well with the experiment and fully support the interpretation that strain is the origin for the decrease in the diffusion barrier (40%) on a compressively strained Ag layer (4.3%) when compared to strain free Ag(111). This result is corroborated by Mortensen et al. who explicitly address the correlation of strain and diffusion barriers and calculate the derivative of E_m with lattice mismatch for several transition metals [125].

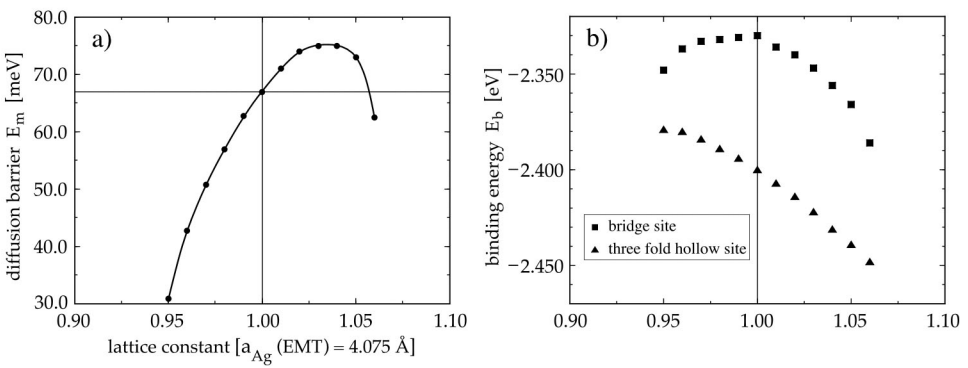

Figure 20. EMT calculations of (a) the barrier for Ag self diffusion on a Ag(111) slab, and (b) binding energies in the transition (bridge) and binding (hollow) sites as a function of tensile or compressive strain. From [9].

The physical reason for the strong influence of strain on the diffusion barrier at a close packed surface can be analyzed on hand of EMT calculations. From Fig. 20b it is seen that the binding energy in the three-fold hollow site increases almost linearly with strain. The binding energy in the transition state, on the other hand, varies only little for strains in the range of ±2%. Since the migration barrier is the difference between these two values, it varies almost linearly in that range; increasing for tensile and decreasing for compressive strain. The decrease of the diffusion barrier induced by compressive strain is mainly caused by a smaller binding energy in the hollow site. As expected, for tensile strain the binding energy in the hollow is increased, which leads to the increase in E_m. For larger compressive strains, migration becomes increasingly fast, the barrier attains half of the unstrained value at 4.8% compression. At high tensile strain (> 3.5%) the transition state drastically decreases its energy which explains the bending of the curve and the second decrease in E_m. This can be understood by the increasing softness of the layer with increasing lattice constant. Thus atoms involved in the bridge configuration corresponding to the transition state can relax more efficiently. The result is that the barrier attains a maximum (75 meV at 3.5% tensile strain) and then it drops upon further increase of the lattice constant. Ab-initio calculations don't find this second decrease of E_m, apart from this they fully support the physical picture derived here from EMT [124].

The experimental results discussed in this Section, although available for only one system so far, suggest that isotropic strain in general may have a pronounced influence on adatom mobilities. This is supported by recent ab-initio calculations performed for self-diffusion on strained fcc(111) surfaces of several metals [125]. For all studied metals (Ni, Pd, Pt, Cu, Ag, Au) the authors find tendencies similar to that of Ag/Pt(111), i.e., decreasing barriers for compressive, and increasing barriers for tensile strain. We will discuss in Section 4.4. below that strain also strongly influences interlayer diffusion. Therefore, the entire nucleation and growth kinetics of heteroepitaxial systems may be dominated by these strain effects.

4.3. Nucleation on anisotropically strained substrates

As has been discussed in Section 2 of this chapter, the strain energy present in heteroepitaxial systems can lead to a transition from pseudomorphic to weakly incommensurate layers. Together with the substrate reconstructions these weakly incommensurate surfaces all have in common non-uniform interatomic distances, i.e., they reveal anisotropic strain. In the preceding Section we have seen how sensitive barriers for surface diffusion depend on isotropic strain, we therefore expect strong effects on the nucleation kinetics also for anisotropic strain. The example for Ni/Ru(0001) (see Fig. 15) already

showed that this is the case. In this Section we will discuss the effect of anisotropic strain in more detail in concentrating on the case of fcc(111) surfaces and the role played by their partial dislocations in nucleation kinetics. We will first show two examples for nucleation on the Au(111) surface with its reconstruction revealing a higher density of surface atoms. In comparison, we discuss an example of nucleation on a surface where the partial dislocations reduce the surface density, i.e., on a regular dislocation network of the second Ag layer on Pt(111).

The (111) surfaces of Au and Pt are known to reconstruct, driven by the considerable tensile stress in the outermost layer. As discussed in detail in Sect. 3.1. these reconstructions consist in the introduction of a certain density of dense domain walls, or partial dislocations, between alternating fcc and hcp stacking regions.

Chambliss and coworkers showed that the "elbows" at the Au(111) surface, where the partial dislocations bend act as sites of preferred nucleation for Ni deposited at room temperature [133-135]. This leads to quite regularly spaced islands accompanied by a narrow island size distribution (see Fig. 21).

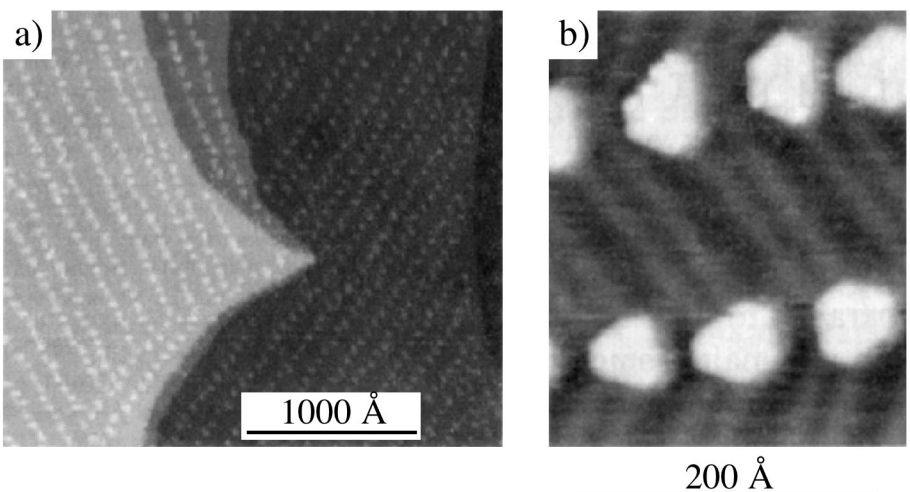

Figure 21. STM images of Ni nucleation on the $(\sqrt{3}x22)$-reconstructed Au(111) surface at room temperature. a) Large scale image showing the monolayer Ni islands aligned in rows along the $\langle 11\bar{2} \rangle$-directions ($\Theta$ = 0.11 ML). b) Detail showing that islands are located at elbows of the herringbone reconstruction (Θ = 0.14 ML). From [133].

Preference of nucleation at, or close to elbows of the Au reconstruction was also observed for room temperature deposition of Fe [136, 137], Co [138], and Rh [139]. The case of Au(111) auto-epitaxy is less clear. In a study by

Chambliss et al., too few islands formed at room temperature precluding statistically significant statements [134]. In contrast, in an earlier work nucleation has been found at elbows, however, in that study the sample was transferred through air which is likely to invoke contamination problems [140]. For Ag, on the other hand, nucleation is homogeneous and independent of the mesoscopic order of the $(\sqrt{3}\text{x}22)$-reconstruction [141, 142]. The same is true for Cu [143] and also for Al as we will discuss below. The distinctive anisotropy of the nucleation probability at elbows of the reconstruction, found so far for Ni, Fe, Co, and Rh, was ascribed by Chambliss et al. in the case of Ni/Au(111) to attractive potential wells located at elbows which effectively trap single diffusing atoms. It has been shown in a Monte-Carlo simulation that already small trapping probabilities at the elbows may be sufficient to cause the experimentally observed alignment of islands [133]. Very recently, the system Ni/Au(111) was revisited evolving an alternative explanation [144]. The authors demonstrated that the Ni adatoms perform a place exchange with Au surface atoms localized at the elbows, followed by preferential nucleation of Ni islands on top of substitutional Ni atoms. The elbows are areas of locally increased strain, since there a close packed atomic row terminates, as directly demonstrated on hand of STM images of these regions [133, 145]. As a result, there is one Au atom with only 5-fold lateral coordination. The reason for preferred place exchange at elbows is thought to be this reduced coordination in these highly strained areas rendering place exchange easier than throughout the terraces.

A necessary condition for preferred nucleation at elbows, or in general at dislocations is that these can be reached by adatoms, which implies that the total binding energy must either stay constant or increase at these sites (the latter would render dislocations attractive). On the other hand, if the binding energy decreases at dislocations, they constitute repulsive barriers that may effectively reflect migrating adatoms. As an example for the latter case we discuss the nucleation of Al again on the reconstructed Au(111) surface at low temperature [146]. From the STM image shown in Fig. 22 it is seen that at 150 K Al islands nucleate in-between the partial dislocations of the otherwise unperturbed reconstructed Au(111) surface. In the Arrhenius plot of the saturation island density there are three regimes of nucleation clearly distinguished by their markedly different slope. For temperatures below 200 K, mean island distances lie below the distance between dislocations. (The corresponding island density is marked by the dashed horizontal line.) This indicates that also the mean free path of diffusing atoms is below this value and the adatoms predominantly diffuse and nucleate on the isotropic fcc and hcp areas and do not see much of the dislocations. For this regime a migration barrier of 30±5 meV is extracted

from the slope under the assumption of isotropic diffusion. This barrier compares well with results from density-functional-theory (DFT) calculations performed by Stumpf and Scheffler yielding a barrier of 40 meV for Al(111) self-diffusion [147]. Notice, however, that for Au(111) self-diffusion a much higher barrier (0.22±0.03 eV) has been calculated also with first principles methods [132].

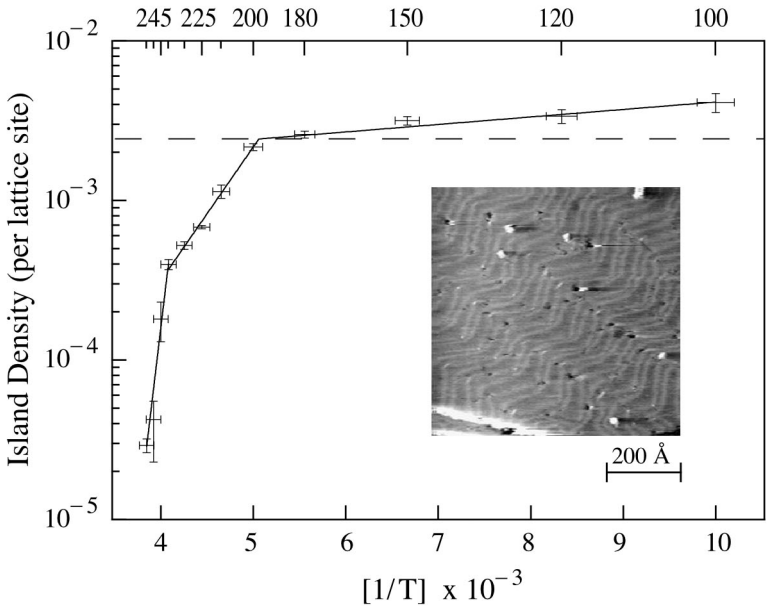

Figure 22. Arrhenius plot of saturation island densities deduced from variable-temperature STM for the nucleation of Al on the $(\sqrt{3}x22)$-reconstructed Au(111) surface (Θ = 0.10 - 0.15 ML, F = 3.1x10^{-4} ML/s). The inset shows that islands nucleate in-between the partial dislocations (Θ = 0.04 ML, T = 150 K, F = 3.1x10^{-4} ML/s). From [146].

At temperatures above 200 K the adatoms cross dislocations as the mean island separation becomes larger than the dimensions of the $(\sqrt{3}x22)$-unit cell. The diffusion over partial dislocations is associated with an increased barrier, reflected in the strongly increased second slope. Here, a quantitative analysis in order to extract an effective barrier for crossing dislocations would require a KMC simulation, since mean-field nucleation theory is no longer applicable for this particular case. We notice, however, that this barrier is significant, compared to the small barrier to diffusion on the pseudomorphic parts of the substrate. The finding that dislocations can represent repulsive barriers is corroborated by EMT calculations performed for Pt/Pt(111) [148]. In these calculations, the binding energy of the Pt adatom is found to be decreased as it

approaches the partial dislocation. Even if the change in total energy is small (half the migration barrier) , it is feasible to lead to drastic changes in diffusivity because atoms have to make successively several jumps into unfavorable directions to overcome a dislocation. This interpretation is supported by experimental evidence for a high effective barrier towards crossing of dislocations for Pt/Pt(111) recently reported from STM observations on the nucleation behavior of this system at 650 K [79]. At temperatures above 400 K the Pt(111) substrate surface is known to reconstruct in the presence of Pt adatoms [32]. The dislocations associated with the reconstruction are observed to lead to a strongly reduced mobility on the reconstructed substrate terraces. Since islands do not reconstruct, the mobility remains high on-top of them (see Fig. 14, we have the case where $D_n >> D_{n-1}$). Together with the fact that the interlayer barrier can readily be overcome above 400 K, this causes the most perfect layer-by-layer growth observed so far [71, 79].

The third nucleation regime of Al/Au(111) sets in at 245 K and is again clearly discerned by its slope in the Arrhenius in Fig. 22. It is due to modification of the reconstruction associated with alloy formation [149]. Alloy formation with the Au(111) surface has also been found for Pd from 240 K on [150], and for Rh on upon annealing to 670 K [139].

A case of nucleation on a regular network of dislocations of reduced density has been reported for Ag nucleation on the second Ag monolayer adsorbed on Pt(111) [9]. The second Ag layer transforms upon annealing to 800 K from a striped incommensurate phase into a trigonal network of crossing dislocations as discussed in detail in Sect. 3.1. Ag nucleation onto this surface at low temperature leads to a high density of islands where the majority is located away from dislocations [9]. This implies that they constitute repulsive barriers as in the preceding example. For increasing temperatures the island density approaches a minimum at 110 K, where only one island forms per network unit cell. Figs. 23 a) and b) show nucleation at 90 K and 110 K with on the average 1.3 and 1.1 islands per unit cell of the superstructure. Note that very few of the islands form on dislocations, the majority nucleate on the hexagons of the unit cell, which are pseudomorphic with fcc stacking [40].

These examples illustrate that dislocations in general strongly influence nucleation. They can constitute rather effective repulsive barriers, leading to an increased island density, even if diffusion on the homogeneously strained parts of the surface may be fast. Dislocations can also act as preferred nucleation sites which can be understood in terms of localized strain which either facilitates exchange or locally increases migration barriers, or binding energies. Whether dislocations act as nucleation sites or reflective barriers for migrating atoms depends on the variation in binding energy, the diffusion barrier when crossing

the dislocation, as well as the tendency to alloy formation, and has to be investigated for each particular system.

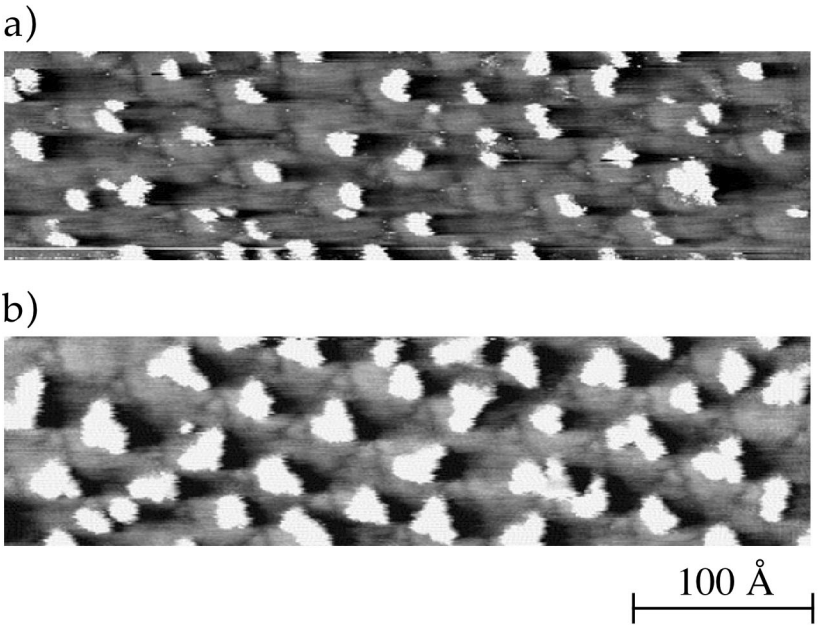

Figure 23. STM images showing nucleation of Ag on a regular trigonal network of dislocations formed by 2 ML Ag/Pt(111) after annealing to 800 K. a) T = 90 K, island density n_x = 1.3 per unit cell of superstructure, Θ = 0.03 ML, **(b)** T = 110 K, n_x = 1.1 per unit cell of superstructure, Θ = 0.12 ML. From [9].

Independent from the respective nature of the interaction, the influence of dislocations and in general anisotropic strain on nucleation can be applied to significantly decrease the width of island size- and distance distributions when compared to nucleation on isotropic substrates. Here, one takes advantage of the fact that there is generally a strong repulsive interaction between dislocations often leading to their arrangement in periodic patterns. Fig. 23b shows that quite regularly spaced islands with a narrow size distribution may result upon nucleation on such a network. Also in moiré patterns, there are periodic variations in strain and/or adatom binding energy which may similarly lead to regular island spacing for nucleation on these layers. It has to be kept in mind, however, that, at least for the case of repulsive barriers, one is confronted with the fact that there is no plateau in temperature for the desired island density of one island per superstructure unit cell but rather a change in slope necessitating the careful choice of the deposition temperature. The influence of anisotropic

strain on surface diffusion can also be the key to understand anisotropic diffusion observed on hex-reconstructed fcc(100) surfaces [95, 96]. Finally, anisotropic strain is in general expected to strongly influence surface diffusion and nucleation. This has direct implications for growth morphologies of heteroepitaxial systems with lattice mismatch and even for homoepitaxial systems when they are unstable upon reconstruction due to their intrinsic tensile stress.

4.4. Strain and interlayer diffusion

When an adatom approaches a descending step, it generally encounters an additional energy barrier for descend. This additional step edge barrier, $\Delta E_s = E_s - E_m$, is the energy barrier for an adatom to descend the step minus the diffusion barrier on a flat terrace (see potential energy diagrams in Fig. 24). Although first experimental evidence for this barrier was observed already 30 years ago by Ehrlich and Hudda [151] and theoretical consequences were discussed at that time by Schwoebel and Shipsey [152, 153], quantitative measurements of ΔE_s are rare [154, 155].

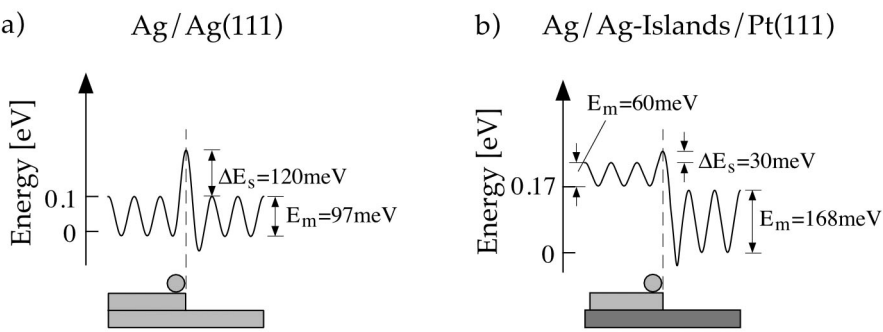

Figure 24. Potential energy diagrams (a) for Ag(111) homo- and (b) for Ag/Pt(111) heteroepitaxy of the first layer. From [10].

In addition to these direct measurements by FIM, there have been various approaches to derive estimates for ΔE_s from the film morphology at a given coverage and temperature, mostly obtained from STM. In the absence of interlayer mass transport the exposed coverages in successive layers obey a Poisson distribution. The deviation of the layer occupancies from this distribution, due to a certain amount of interlayer transport, can be analyzed to estimate the additional step edge barrier. For this purpose typically a linear model for interlayer mass transport [156] is applied. In recent literature, this model has been refined to account for layer dependent interlayer [74] and also

intralayer diffusivity [157, 158]. Also a model based on the critical coverage for second layer nucleation has been applied to STM data [158].

Recently, Tersoff et al. used mean-field nucleation theory to show that the nucleation rate on-top of islands reveals a sharp transition from 0 to 1 with increasing island radius [159]. Based on this approach, a general method for the quantitative determination of the additional step edge barrier was developed [10]. From the measurement of the nucleation rate on-top of previously grown islands as a function of their size and substrate temperature, ΔE_s and the corresponding attempt frequency can be inferred with high accuracy. As ingredients, one needs to know the parameters for terrace diffusion and the critical cluster size on-top of the islands.

We discuss this method for the example of Ag(111) homoepitaxy which has frequently been addressed in recent literature [10, 74, 160, 161]. It reveals a considerable additional step edge barrier [10, 157, 158] and thus grows 3D below 400 K while it grows 2D (step flow) at elevated temperatures [74]. We will compare the results to Ag heteroepitaxy on Pt(111). As in the case of terrace diffusion, also interlayer diffusion is strongly influenced by strain.

A fist step for the experiment is the preparation of a high abundance of circular 2D islands with a size distribution sufficiently broad to enable the study of the nucleation rate on-top of these islands as a function of their size. Such a distribution of islands can be synthesized in a simple way via Ostwald ripening [107]. Fig. 24 shows STM images of 2D Ag islands grown on a Pt(111) surface by annealing dimers and trimers created from a low temperature deposition experiment. There is a clear threshold temperature for the onset of Ostwald ripening as inferred from the graph in Fig. 25. This temperature is 100 K in our case of annealing periods lasting half an hour. This threshold bears valuable information on critical cluster sizes and their mobility; since dimer (and trimer) dissociation and their mobility would lead to detectable island coarsening, both can be excluded below this threshold. Annealing to higher temperatures leads to an exponential increase in mean island size due to Ostwald ripening, i.e., stronger evaporation from smaller islands leading to their decay in favor of larger ones. The islands of 6, 14, and 200 atoms average size are to a good approximation circular. Those containing 800 atoms on the average begin to approach the thermodynamic equilibrium shape, i.e., a distorted hexagon with the two kinds of close packed steps having different length's according to their free energy difference [107, 114].

The size distributions of Ostwald ripening satisfy a scaling law and are by a factor of 2 more narrow than those obtained from nucleation experiments [108]. As we will see below, the width is still sufficient to study the nucleation rate as a function of island size. Notice that this method of preparation of circular islands

by Ostwald ripening is generally applicable to a any epitaxial system that does not show intermixing at the required annealing temperatures.

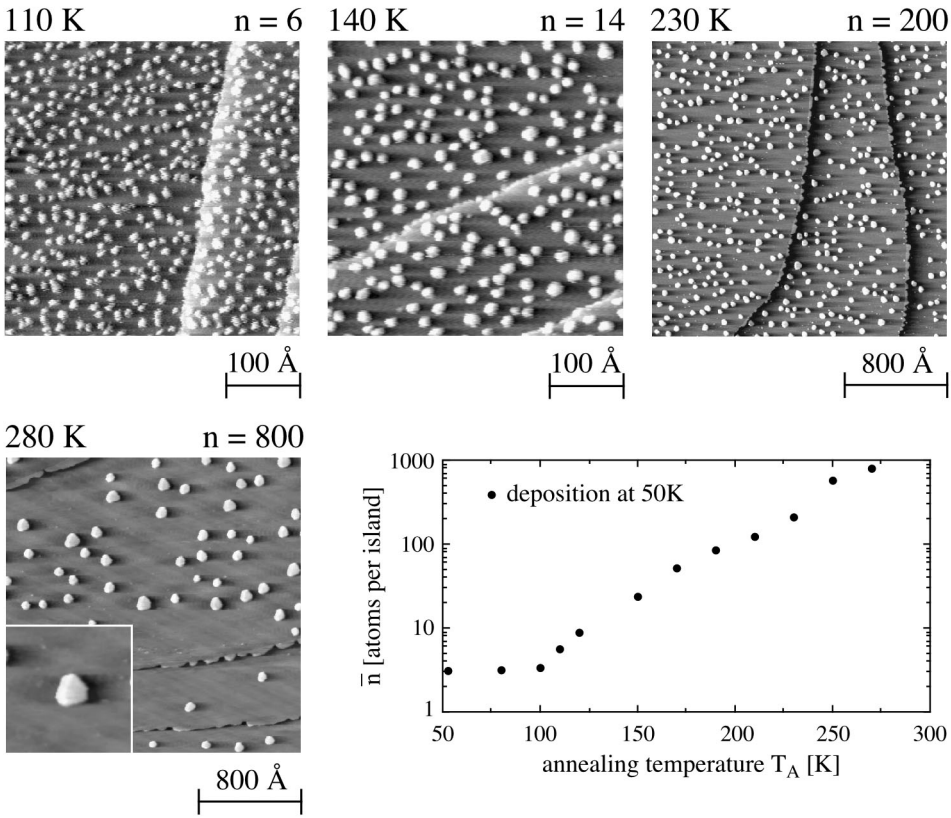

Figure 25. STM images showing that compact 2D Ag islands with defined sizes are obtained via deposition of 0.1 ML Ag at 50 K on Pt(111) and subsequent annealing. The graph shows the exponential increase of the mean island size with annealing temperature due to Ostwald ripening. From [107].

To study the nucleation probability on these well prepared 2D islands, a submonolayer coverage is then deposited in a second step at a certain temperature. As can be seen from Fig. 26 only a fraction of the preexisting islands reveal second layer islands on-top, the smaller islands are mostly bare of second layer nuclei. In addition, the critical size for second layer nucleation increases with increasing temperature (compare Fig. 26 a and b, where the second deposition step has been performed at 60 K and 85 K, respectively). Due to the low coverage of the preexistent islands most of the deposited material

lands on the substrate surface (in our example 90%). These atoms then either form additional islands in-between those prepared by Ostwald ripening, as the case in Fig. 26, or they attach to the preexisting islands and contribute to their growth. These two cases will have to be distinguished in the analysis described below.

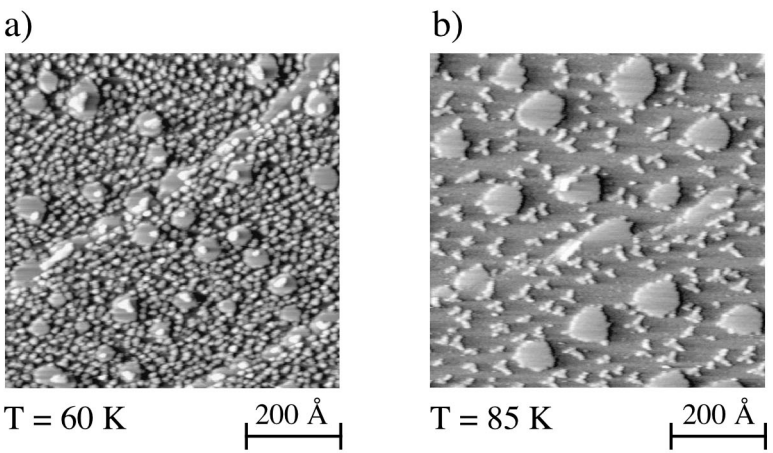

Figure 26. STM images showing the results of nucleation experiments, in which 0.1 ML Ag were deposited ($F = 1.3 \times 10^{-3}$ ML/s) on compact 2D Ag islands that have previously been prepared by Ostwald ripening on Pt(111). From [10].

The fraction of islands revealing second layer nucleation deduced from a large number of STM experiments, taken out at three different temperatures, is shown in two graphs in Fig. 27 for the case of Ag homoepitaxy and Ag/Pt(111) heteroepitaxy, respectively. It is clearly seen that there is a well defined transition for the nucleation probability from 0 to 1 as the island size increases. The curves show the best fits to the experiment resulting from a calculation applying mean-field nucleation theory [159]. This theory yields that the nucleation rate on-top of an adisland strongly depends on the 2D monomer density that builds up there (to the power of the stable island size).

Under steady state conditions, i.e., the incident atom flux onto an island equals the downward flux from that island at its perimeter, and for circular islands, this density has a parabolic radial dependence. Its maximum is located at the island center and determined by the island size and the ratio of interlayer- to terrace diffusion. This ratio is given by $\exp(-\Delta E_s/kT)$, where ΔE_s is the additional step edge barrier introduced above. Integrating the nucleation rate over the island area in course of deposition yields the curves shown in Fig. 27. Depending on the mean-free path of adatoms on the substrate compared to the

mutual distance of the preexistent islands these may grow during the second deposition step due to diffusion and attachment of material that has been deposited on the substrate. This can be accounted for in including a variation of island size when integrating the nucleation rate over time [10].

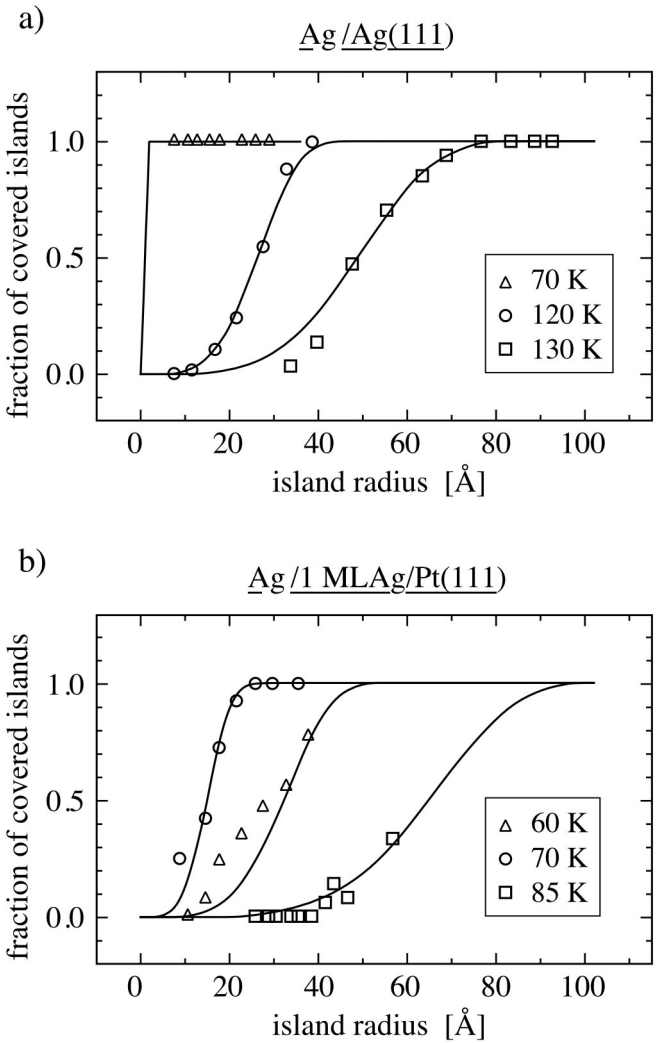

Figure 27. Quantitative evaluation of the nucleation probability for Ag in 2D Ag islands on Ag(111) (a) and Pt(111) (b). The fraction of covered islands is shown as a function of island radius and deposition temperature determined from STM experiments in comparison to theoretical curves representing the best fits. From [10].

In analyzing STM data obtained at various temperatures one can clearly separate the attempt frequency form the additional barrier for interlayer diffusion. The first predominantly shifts the whole set of curves along the abscissa in Fig. 27, whereas the latter largely determines the horizontal distance between the curves for the various temperatures. The fits are rather sensitive to the only free parameters, ν_0 and ΔE_s, especially to the choice of ΔE_s, which in turn allows its precise determination.

For Ag homoepitaxy an additional step edge barrier of $\Delta E_s = 120 \pm 15$ meV is obtained with this method. This is higher than the Ag adatom diffusion barrier of 97 meV (see Fig. 24) and explains the 3D growth of the homoepitaxial system experimentally observed below 400K [74]. The values estimated for Ag(111) in previous studies, either from layer occupancies (150±20 meV) [157] or from the critical coverage at the onset of second layer nucleation (0.19 - 0.23 eV) [158], are both slightly higher than the value for ΔE_s determined above. Both evaluations are based on STM data obtained at a single temperature and therefore presumably reveal higher uncertainties than the value derived above from the temperature dependence of the nucleation rate on-top of preexistent islands.

The additional activation energy for step-down diffusion in the strained heteroepitaxial system Ag/Ag islands/Pt(111) is determined to $\Delta E_s = 30 \pm 5$ meV. This is only 25% of the barrier in the homoepitaxial case and thus remarkably small. There are two differences to the homoepitaxial case which are conceivable to cause the observed lowering of ΔE_s. While in homoepitaxy both, upper and lower terrace are energetically on the same level, energy levels of successive layers may be different in heteroepitaxy. In the case of Ag/Pt(111) the binding energy for an Ag adatom on the 1st Ag layer is about 170 meV lower than on the Pt(111) substrate [126] (see Fig. 24). This energy difference might be thought to bend down the potential at the step, implying, however, that the energy gain must be available to the descending atom already in its transition state. Whether this is reasonable certainly depends on the microscopic mechanism for descend. The second difference with respect to Ag(111) homoepitaxy is the substantial compressive strain of 4.3% inherent in the 1st Ag layer on Pt(111) [10]. The pseudomorphic islands preferentially relieve their strain at the edges where the Ag atoms are free to expand laterally. This edge relaxation can certainly favor exchange processes which have been suggested as the mechanism associated with the lowest barrier for atom descend on fcc(111) surfaces [129, 147, 162]. The strain argument is strongly corroborated by the observation that the low interlayer barrier is only observed where the Ag layer is free to relax at its edge. If this is not the case, e.g., where the Ag layer touches a former Pt step, atom descend is inhibited leading to the formation of pin holes at

steps [36]. Similarly to the first Ag layer, descend from the second Ag layer is found to have a reduced additional barrier of ΔE_s = 60±20 meV as estimated from layer occupancies [36]. Presumably, also here the strain still present in the second layer is causing the slightly reduced barrier with respect to the strain free Ag(111) case.

Strain can also be thought to be involved in the decrease of ΔE_s caused by certain surfactants. As an example we consider the oxygen mediated layer-by-layer growth of Pt/Pt(111) [163]. Pt islands on Pt(111) are under tensile stress. Chemisorption of an electronegative adsorbate like oxygen at the island edge weakens the lateral bond of the edge atoms towards the island. This manifests itself in a detectable outward relaxation of the edge atoms [164]. Outward displacement of edge atoms constitutes the first step to adatom descend by exchange. Therefore, the outward relaxation of edges, either by strain or by electronegative adsorbates, can lower the barrier to interlayer diffusion.

Notice, all values for interlayer diffusion discussed here represent *effective barriers*, they can not unambiguously be assigned to a microscopic diffusion process. These effective barriers, however, determine the growth morphology in a real deposition experiment and its precise measurement with the method outlined above is therefore rather valuable. The nucleation rate method is an alternative to FIM measurements for the determination of ΔE_s. FIM studies generally allow to trace the atoms in their initial and final state before and after descend, in order to find the microscopic pathway. However, for interlayer diffusion, this is often hampered by edge diffusion immediately following descend [155]. In some cases, the effective barriers measured with the nucleation method can be related to a microscopic process. If there is an interlayer process associated with a particularly low barrier, than the measured effective barrier presumably reflects the activation energy for this most efficient process. For close packed surfaces, e.g., the process associated with the lowest barrier is likely to be exchange at B-steps, since there atoms move out more easily than at straight A-steps.

The example of Ag/Pt(111) shows that the step-edge barrier on the pseudomorphic Ag-islands is found to be substantially lowered with respect to the homoepitaxial system. This lowering is related to relaxation effects at the edges of the compressively strained islands. It is likely that stain in general strongly influences adatom descend at steps. Due to the example discussed here compressive strain facilitates interlayer diffusion, which presumably takes place through exchange on fcc(111) surfaces. It is certainly very interesting to apply the method for the quantitative measurement of ΔE_s described above to further study the influence of strain on interlayer diffusion. The results obtained so far, clearly indicate that strain effects can cause layer dependent interlayer barriers

which will have to be taken into account for modeling the kinetics in heteroepitaxial growth.

Within the recent years considerable progress has been made in the quantitative understanding of the microscopic processes involved in epitaxial growth. New methods have been developed to determine their activation energies. They rely on the application of mean-field nucleation theory or Kinetic Monte-Carlo simulations to island densities obtained from measurements with variable-temperature STM. This technique supplements FIM measurements which so far have been the most important and precise source for activation energies for diffusion of single particles. Other than FIM, the new approach with variable temperature STM allows to study strain effects and diffusion on large areas. The examples reviewed in this Section are the first experimental indication that strain has a pronounced effect on terrace, as well as on interlayer diffusion. The activation energies obtained for various systems with this new technique are valuable for comparison with theoretical calculations which in the past improved considerably concerning absolute values. Together with theory, the recent progress in experimental study of the relevant microscopic processes has certainly increased our understanding of the kinetics of epitaxial growth.

ACKNOWLEDGEMENTS

We gratefully acknowledge valuable contributions of C. Boragno, K. Bromann, J. P. Bucher, B. Fischer, A. Fricke, E. Hahn, E. Kampshoff, B. Müller, L. Nedelmann, H. Röder, C. Romainczyk, and N. Wälchli to the experimental results presented here. We also acknowledge collaboration with J. Jacobsen, K. W. Jacobsen, P. Stoltze, and J. Nørskov in performing simulations with Effective Medium Theory, as well as with G. S. Bales concerning nucleation theory.

REFERENCES

1. J. Thomassen, B. Feldmann and M. Wuttig, Surf. Sci. **264**, 406 (1992).
2. M. Straub, B. Vollmer and J. Kirschner, Phys. Rev. Lett. **77**, 743 (1996).
3. F. C. Frank and J. H. v. d. Merwe, Proc. R. Soc. London A **198**, 205 (1949).
4. J. W. Matthews and A. E. Blakeslee, J. Cryst. Growth **27**, 118 (1974).
5. R. J. Asaro and W. A. Tiller, Metall. Trans. **3**, 1789 (1972).
6. M. A. Grinfeld, Sov. Phys. Dokl. **31**, 831 (1986).
7. M. A. Hermann and H. Sitter, *Molecular Beam Epitaxy* (Springer, Berlin, 1989).
8. G. Rosenfeld, H. Lipkin, W. Wulfhekel, J. Kliewer, K. Morgenstern, B. Poelsema and G. Comsa, Appl. Phys. A **61**, 455 (1995).

9. H. Brune, K. Bromann, H. Röder, K. Kern, J. Jacobsen, P. Stolze, K. Jacobsen and J. Nørskov, Phys. Rev. B **52**, R14380 (1995).
10. K. Bromann, H. Brune, H. Röder and K. Kern, Phys. Rev. Lett. **75**, 677 (1995).
11. H. Brune, K. Bromann and K. Kern, Mat. Res. Soc. Symp. Proc. **399**, 213 (1995).
12. E. Bauer, Z. Kristallogr. **110**, 372 (1958).
13. R. Kern, G. L. Lay and J. J. Métois, in *Current Topics in Materials Science*, vol. 3, E. Kaldis, Eds. (Amsterdam, North-Holland, 1979), p. 131.
14. D. E. Sullivan, Phys. Rev. B **20**, 3991 (1979).
15. M. Bienfait, J. L. Senguin, J. Suzanne, E. Lerner, J. Krim and J. G. Dash, Phys. Rev. B **29**, 983 (1984).
16. K. Kern and C. Comsa, in *Kinetics of Ordering and Growth at Surfaces*, vol. M. G. Lagally, Eds. (Plenum Press, New York, 1990), p. 53.
17. E. Bauer and J. H. V. d. Merwe, Phys. Rev. B **33**, 3657 (1986).
18. M. H. Grabow and G. H. Gilmer, Surf. Sci. **194**, 333 (1988).
19. J. Frenkel and T. Kontorova, Zh. Eksp. Teor. Fiz. **8**, 1340 (1939).
20. J. H. v. d. Merwe, J. Appl. Phys. **34**, 117 (1963).
21. W. A. Jesser and D. Kuhlmann-Wilsdorf, Phys. Status Solidi **42**, 357 (1970).
22. J. W. Matthews, *Epitaxial Growth*, vol. B, (Academic Press, New York, 1975).
23. H. Brune, H. Röder, C. Boragno and K. Kern, Phys. Rev. B **49**, 2997 (1994).
24. C. Günther, J. Vrijmoeth, R. Q. Hwang and R. J. Behm, Phys. Rev. Lett. **74**, 754 (1995).
25. J. A. Meyer, P. Schmid and R. J. Behm, Phys. Rev. Lett. **74**, 3864 (1995).
26. B. Müller, B. Fischer, L. Nedelmann, A. Fricke and K. Kern, Phys. Rev. Lett. **76**, 2358 (1995).
27. B. Müller, L. Nedelmann, B. Fischer, A. Fricke and K. Kern, J. Vac. Sci. Technol. **A 14**, 1878 (1996).
28. R. Q. Hwang, J. C. Hamilton, J. L. Stevens and S. M. Foiles, Phys. Rev. Lett. **75**, 4242 (1995).
29. J. Perdereau, J. P. Biberian and G. E. Rhead, J. Phys. F **4**, 798 (1974).
30. Y. Tanishiro, H. Kanamori, K. Takayanagi, K. Yagi and G. Honjo, Surf. Sci. **111**, 395 (1981).
31. A. R. Sandy, S. G. J. Mochrie, D. M. Zehner, G. Grübel, K. G. Huang and D. Gibbs, Phys. Rev. Lett. **68**, 2192 (1992).
32. M. Bott, M. Hohage, T. Michely and G. Comsa, Phys. Rev. Lett. **70**, 1489 (1993).
33. J. V. Barth, H. Brune, G. Ertl and R. J. Behm, Phys. Rev. B **42**, 9307 (1990).
34. S. Narasimhan and D. Vanderbilt, Phys. Rev. Lett. **69**, 1564 (1992).
35. U. Harten, A. M. Lahee, J. P. Toennies and C. Wöll, Phys. Rev. Lett. **54**, 2619 (1985).
36. H. Röder, K. Bromann, H. Brune and K. Kern, Surf. Sci. in press (1996).
37. C. Wöll, S. Chiang, R. J. Wilson and P. H. Lippel, Phys. Rev. B **39**, 7988 (1989).
38. G. O. Pötschke and R. J. Behm, Phys. Rev. B **44**, 1442 (1991).
39. J. C. Hamilton and S. M. Foiles, Phys. Rev. Lett. **75**, 882 (1995).
40. G. Rangelov, T. Fauster, U. Strüber and J. Küppers, Surf. Sci. (Proc. ECOSS-14) **331-333**, 948 (1995).
41. Notice, the first monolayer of Ag on Pt(111) grows only pseudomorphic when either completed or present as small islands. When the islands reach a certain size the formation of dislocations is observed. Interestingly, these dislocations disappear again upon completion of the first layer.
42. K. Bromann, M. Giovanini, H. Brune and K. Kern, to be published.

43. M. Horn-von-Hoegen, A. A. Falou, H. Pietsch, B. H. Müller and M. Henzler, Surf. Sci. in press (1993).
44. J. Barth, R. J. Behm and G. Ertl, Surf. Sci. **341**, 62 (1995).
45. M. Böhringer, P. Molinàs-Mata, E. Artacho and J. Zegenhagen, Phys. Rev. B **51**, 9965 (1995).
46. E. Artacho, P. Molinàs-Mata, M. Böhringer, J. Zegenhagen, G. E. Franklin and J. R. Patel, Phys. Rev. B **51**, 9952 (1995).
47. C. Romainczyk, Ph. D., Ecole Polytechnique Fédérale de Lausanne, (1994).
48. C. Nagl, M. Schmid and P. Varga, Surf. Sci. to be published (1996).
49. R. Feidenhans'l, Surf. Sci. Rep. **10**, 105 (1989).
50. Monatomic Cu chains on a Pd(110) surface are usually imaged with a width of ≈ 5 - 8 Å; J. P. Bucher, E. Hahn, P. Fernandez, C. Massobrio and K. Kern, Europhys. Lett. **27**, 473 (1994).
51. S. A. Chambers, H. W. Chen, I. M. Vitomirov, S. B. Anderson and J. H. Weaver, Phys. Rev. B **33**, 8810 (1986).
52. J. W. Matthews and J. L. Crawford, Thin Solid Films **5**, 178 (1970).
53. E. C. Bain, Trans. AIME **70**, 25 (1924).
54. I. A. Morrison, M. H. Kang and E. J. Mele, Phys. Rev. B **39**, 1575 (1989).
55. H. Li, S. C. Wu, D. Tian, J. Quinn, Y. S. Li, F. Jona and P. M. Marcus, Phys. Rev. B **40**, 5841 (1989).
56. T. Kraft, P. M. Marcus, M. Methfessel and M. Scheffler, Phys. Rev. B **48**, 5886 (1993) and references [4-6] therein.
57. Y. S. Li, S. C. Wu, D. Tian, J. Quinn, H. Li, F. Jona and P. M. Marcus, Phys. Rev. B **44**, 8261 (1991).
58. E. Hahn, E. Kampshoff, N. Wälchli and K. Kern, Phys. Rev. Lett. **74**, 1803 (1995).
59. S. Jeong, Phys. Rev. B **53**, 13973 (1996).
60. J. G. Dash, J. Vac. Sci. Technol. A **5**, 1523 (1986).
61. E. Hahn, E. Kampshoff, A. Fricke, J. P. Bucher and K. Kern, Surf. Sci. **319**, 277 (1994).
62. J. Villain, A. Pimpinelli and D. E. Wolf, Comments Cond. Mater Phys. **16**, 1 (1992).
63. J. Villain, A. Pimpinelli, L. Tang and D. Wolf, J. Phys. France **2**, 2107 (1992).
64. G. Rosenfeld, B. Poelsema and G. Comsa, J. Cryst. Growth **151**, 230 (1995).
65. These arguments only hold for low index surface planes which have low surface free energies. On higher index planes faceting might be thermodynamically favored.
66. C. S. Lent and P. J. Cohen, Surf. Sci. **139**, 121 (1984).
67. J. Zhang, J. H. Neave, B. A. Joyce, P. J. Bobson and P. N. Fawcett, Surf. Sci. **231**, 379 (1990).
68. J. M. V. Hove, C. S. Lent, P. R. Pukite and P. I. Cohen, J. Vac. Sci. Technol. B **1**, 741 (1983).
69. W. F. Egelhoff and I. Jacob, Phys. Rev. Lett. **62**, 921 (1989).
70. K. D. Gronwald and M. Henzler, Surf. Sci. **117**, 180 (1982).
71. R. Kunkel, B. Poelsema, L. K. Verheij and G. Comsa, Phys. Rev. Lett. **65**, 733 (1990).
72. L. J. Gomez, S. Bourgeal, J. Ibanez and M. Salmeron, Phys. Rev. B **31**, 255 (1985).
73. E. Vlieg, A. W. D. v. d. Gon, J. F. V. d. Veen, J. E. MacDonald and C. Norris, Phys. Rev. Lett. **61**, 2241 (1988).
74. H. A. v. d. Vegt, H. M. v. Pinxteren, M. Lohmeier, E. Vlieg and J. M. Thornton, Phys. Rev. Lett. **68**, 3335 (1992).
75. S. V. Ghaisas, Surf. Sci. **223**, 441 (1989).
76. C. Roland and G. H. Gilmer, Phys. Rev. B **46**, 13428 (1992).

77. C. Ratsch and A. Zangwill, Appl. Phys. Lett. **63**, 2348 (1993).
78. H. Spjut and D. A. Faux, Surf. Sci. **306**, 233 (1994).
79. T. Michely, M. Hohage, S. Esch and G. Comsa, Surf. Sci. **349**, L89 (1996).
80. G. Ehrlich, Surf. Sci. **246**, 1 (1991).
81. G. L. Kellogg, Surf. Sci. Rep. **21**, 1 (1994).
82. J. A. Venables, G. D. T. Spiller and M. Hanbücken, Rep. Prog. Phys. **47**, 399 (1984).
83. G. Binnig and H. Rohrer, Helv. Phys. Acta **55**, 726 (1982).
84. G. Binnig, H. Rohrer, C. Gerber and E. Weibel, Phys. Rev. Lett. **49**, 57 (1982).
85. H. Dürr, J. F. Wendelken and J. K. Zuo, Surf. Sci. **328**, L527 (1995).
86. H. J. Ernst, F. Fabre and J. Lapujoulade, Phys. Rev. B **46**, 1929 (1992).
87. J. A. Stroscio, D. T. Pierce and R. A. Dragoset, Phys. Rev. Lett. **70**, 3615 (1993).
88. Y. W. Mo, J. Kleiner, M. B. Webb and M. G. Lagally, Phys. Rev. Lett. **66**, 1998 (1991).
89. J. A. Stroscio and D. T. Pierce, Phys. Rev. B **49**, 8522 (1994).
90. M. Bott, T. Michely and G. Comsa, Surf. Sci. **272**, 161 (1992).
91. H. Röder, H. Brune, J. P. Bucher and K. Kern, Surf. Sci. **298**, 121 (1993).
92. H. Brune, H. Röder, C. Boragno and K. Kern, Phys. Rev. Lett. **73**, 1955 (1994).
93. M. Bott, M. Hohage, M. Morgenstern, T. Michely and G. Comsa, Phys. Rev. Lett. **76**, 1304 (1995).
94. J. P. Bucher, E. Hahn, P. Fernandez, C. Massobrio and K. Kern, Europhys. Lett. **27**, 473 (1994).
95. S. Günther, E. Kopatzki, M. C. Bartelt, J. W. Evans and R. J. Behm, Phys. Rev. Lett. **73**, 553 (1994).
96. T. R. Linderoth, J. J. Mortensen, K. W. Jacobsen, E. Laegsgaard, I. Stensgaard and F. Besenbacher, Phys. Rev. Lett. **77**, 87 (1996).
97. J. W. Evans and M. C. Bartelt, J. Vac. Sci. Technol. **A 12**, 1800 (1994).
98. J. Frenkel, Z. Phys. **26**, 117 (1924).
99. G. Zinsmeister, Vacuum **16**, 529 (1966).
100. B. Lewis and D. S. Campbell, J. Vac. Sci. Technol. **4**, 209 (1967).
101. B. Lewis, Surf. Sci. **21**, 289 (1970).
102. B. Lewis and J. C. Anderson, *Nucleation and Growth of Thin Films* (Academic Press, New York, San Francisco, London, 1978).
103. M. J. Stowell, Phil. Mag. **26**, 361 (1972).
104. J. A. Venables, Philos. Mag. **17**, 697 (1973).
105. S. Stoyanov and D. Kashchiev, in *Current Topics in Material Sciences*, vol. 7, E. Kaldis, Eds. (Amsterdam, North Holland, 1981), p. 69.
106. G. S. Bales and D. C. Chrzan, Phys. Rev. B **50**, 6057 (1994).
107. H. Röder, E. Hahn, H. Brune, J. P. Bucher and K. Kern, Nature **366**, 141 (1993).
108. H. Brune, S. Bales, J. Jacobsen, C. Boragno and K. Kern, to be published.
109. T. A. Witten and L. M. Sander, Phys. Rev. Lett. **47**, 1400 (1981).
110. T. A. Witten and L. M. Sander, Phys. Rev. B **27**, 5686 (1983).
111. H. Brune, C. Romainczyk, H. Röder and K. Kern, Nature **369**, 469 (1994).
112. H. Brune, K. Bromann, J. Jacobsen, K. Jacobsen, P. Stoltze, J. Nørskov and K. Kern, Surf. Sci. Lett. **349**, L115 (1996).
113. M. Hohage, M. Bott, M. Morgenstern, Z. Zhang, T. Michely and G. Comsa, Phys. Rev. Lett. **76**, 2366 (1995).
114. T. Michely and G. Comsa, Surface Science **256**, 217 (1991).
115. H. Brune, K. Bromann, J. Jacobsen, K. Jacobsen, P. Stoltze, J. Nørskov and K. Kern, Mat. Res. Soc. Symp. Proc. **407**, 379 (1995).

116. Z. Zhang, X. Chen and M. G. Lagally, Phys. Rev. Lett. **73**, 1829 (1994).
117. B. Müller, B. Fischer, L. Nedelmann, H. Brune and K. Kern, Phys. Rev. B in press (1996).
118. M. C. Bartelt and J. W. Evans, Phys. Rev. B **46**, 12675 (1992).
119. D. E. Wolf, in *Scale Invariance, Interfaces, and Non-Equilibrium Dynamics*, vol. M. Droz, K. J. McKane, J. Vannimenus and D. E. Wolf, Eds. (Plenum, New York, 1994), p. 1.
120. J. G. Amar, F. Family and P. M. Lam, Phys. Rev. B **50**, 8781 (1994).
121. J. G. Amar and F. Family, Phys. Rev. Lett. **74**, 2066 (1995).
122. G. Zinsmeister, Thin Solid Films **7**, 51 (1971).
123. M. J. Stowell, Phil. Mag. **26**, 349 (1972).
124. C. Ratsch and M. Scheffler (private communication).
125. J. J. Mortensen, B. Hammer, O. H. Nielsen, K. W. Jacobsen and J. K. Nørskov, in *Solid State Sciences Series*, vol. 121, A. Okiji, Eds. (Springer, 1996), in press.
126. T. Härtel, U. Strüber and J. Küppers, Thin Sol. Films **229**, 163 (1993).
127. K. W. Jacobsen, J. K. Nørskov and M. J. Puska, Phys. Rev. B **35**, 7423 (1987).
128. P. Stoltze, J. Phys. Condens. Matter **6**, 9495 (1994).
129. J. Jacobsen, K. W. Jacobsen, P. Stoltze and J. K. Nørskov, Phys. Rev. Lett. **74**, 2295 (1995).
130. P. J. Feibelman, J. S. Nelson and G. L. Kellogg, Phys. Rev. B **49**, 10548 (1994).
131. P. J. Feibelman, Surf. Sci. **313**, L801 (1994).
132. G. Boisvert, L. J. Lewis, M. J. Puska and R. M. Nieminen, Phys. Rev. B **52**, 9078 (1995).
133. D. D. Chambliss, R. J. Wilson and S. Chiang, Phys. Rev. Lett. **66**, 1721 (1991).
134. D. D. Chambliss, R. J. Wilson and S. Chiang, J. Vac. Sci. Technol. B **9**, 933 (1991).
135. D. D. Chambliss, K. E. Johnson, R. J. Wilson and S. Chiang, J. Magn. and Magn. Mat. **121**, 1 (1993).
136. B. Voigtländer, G. Meyer and N. M. Amer, Surf. Sci. **255**, L529 (1991).
137. J. A. Stroscio, D. T. Pierce, R. A. Dragoset and P. N. First, J. Vac. Sci. Technol. A **10**, 1981 (1992).
138. B. Voigtländer, G. Meyer and N. M. Amer, Phys. Rev. B **44**, 10354 (1991).
139. E. I. Altman and R. J. Colton, Surf. Sci. **304**, L400 (1994).
140. C. A. Lang, M. M. Dovek, J. Nogami and C. F. Quate, Surf. Sci. **224**, L947 (1989).
141. M. M. Dovek, C. A. Lang, J. Nogami and C. F. Quate, Phys. Rev. B **40**, 11973 (1989).
142. D. D. Chambliss and R. J. Wilson, J. Vac. Sci. Technol. B **9**, 928 (1991).
143. M. Ruff, M. Hugenschmidt and R. J. Behm, to be published.
144. J. A. Meyer, J. D. Baikie, E. Kopatzki and R. J. Behm, to be published.
145. J. V. Barth, PhD-thesis, Freie Universität Berlin, (1992).
146. B. Fischer, L. Nedelmann, A. Fricke, J. Barth, B. Müller, H. Brune and K. Kern, to be published.
147. R. Stumpf and M. Scheffler, Phys. Rev. Lett. **72**, 254 (1994).
148. J. Jacobsen, K. W. Jacobsen and P. Stoltze, Surf. Sci. **317**, 8 (1994).
149. B. Fischer, J. V. Barth, A. Fricke, L. Nedelmann and K. Kern, to be published.
150. B. E. Koel, A. Sellidj and M. T. Paffett, Phys. Rev. B **46**, 7846 (1992).
151. G. Ehrlich and F. G. Hudda, J. Chem. Phys. **44**, 1039 (1966).
152. R. L. Schwoebel and E. J. Shipsey, J. Appl. Phys. **37**, 3682 (1966).
153. R. L. Schwoebel, J. Appl. Phys. **40**, 614 (1969).
154. D. W. Bassett, Surf. Sci. **53**, 74 (1975).

155. S. C. Wang and T. T. Tsong, Surf. Sci. **121**, 85 (1982).
156. P. I. Cohen, G. S. Petrich, P. R. Pukite and G. J. Whaley, Surf. Sci. **216**, 222 (1989).
157. J. A. Meyer, J. Vrijmoeth, H. A. v. d. Vegt, E. Vlieg and R. J. Behm, Phys. Rev. B **51**, 14790 (1995).
158. P. Smilauer and S. Harris, Phys. Rev. B **51**, 14798 (1995).
159. J. Tersoff, A. W. D. v. d. Gon and R. M. Tromp, Phys. Rev. Lett. **72**, 266 (1994).
160. G. Rosenfeld, R. Servaty, C. Teichert, B. Poelsema and G. Comsa, Phys. Rev. Lett. **71**, 895 (1993).
161. J. Vrijmoeth, H. A. v. d. Vegt, J. A. Meyer, E. Vlieg and R. J. Behm, Phys. Rev. Lett. **72**, 3843 (1994).
162. Y. Li and A. E. DePristo, Surf. Sci. **319**, 141 (1994).
163. S. Esch, M. Hohage, T. Michely and G. Comsa, Phys. Rev. Lett. **72**, 518 (1994).
164. F. Sette, T. Hashizume, F. Comin, A. A. MacDowell and P. H. Citrin, Phys. Rev. Lett. **61**, 1384 (1988).